

High-Fidelity Electron Spin Gates in a Scalable Diamond Quantum Register

T. Joas¹, F. Ferlemann², R. Sailer¹, P.J. Vetter¹, J. Zhang¹, R. S. Said¹, T. Teraji³, S. Onoda⁴, T. Calarco^{2,5,6}, G. Genov¹, M. M. Müller², F. Jelezko^{1,7}

¹ Institute for Quantum Optics, Ulm University, 89081 Ulm, Germany

² Peter Grünberg Institute - Quantum Control (PGI-8), Forschungszentrum Jülich GmbH, 52428 Jülich, Germany

³ Research Center for Electronic and Optical Materials, National Institute for Materials Science, Tsukuba, Ibaraki 305-0044, Japan

⁴ Takasaki Advanced Radiation Research Institute, National Institutes for Quantum Science and Technology (QST), Takasaki, Japan

⁵ Institute for Theoretical Physics, University of Cologne, 50937 Köln, Germany

⁶ Dipartimento di Fisica e Astronomia, Università di Bologna, 40127 Bologna, Italy

⁷ Center for Integrated Quantum Science and Technology (IQST), Ulm University, 89081 Ulm, Germany

Diamond is a promising platform for quantum information processing as it can host highly coherent qubits that might allow for the construction of large quantum registers. A prerequisite for such devices is a coherent interaction between electron nitrogen vacancy (NV) spins. Entanglement between dipolar-coupled NV spin pairs has been demonstrated, but with a limited entanglement fidelity and its error sources have not been characterized.

Here, we design a robust, easy to implement entangling gate between NV spins in diamond and quantify the influence of multiple error sources on the gate performance. Experimentally, we demonstrate a record gate fidelity of $F = (96.0 \pm 2.5) \%$ under ambient conditions. Our identification of the dominant errors paves the way towards NV-NV gates beyond the error correction threshold.

Introduction

Quantum processors have evolved from a scientifically intriguing concept into powerful devices on the verge of solving certain computational problems efficiently¹⁻³. Their success has been enabled by the increased number of controllable qubits on recent devices, which can reach three digits numbers^{3,4}. While the steep increase in the number of qubits is formidable, it has come at the cost of reduced gate fidelities as the complexity of routing classical control lines to many qubits rises. In turn, high fidelity devices supporting error correction have featured only modest size⁵⁻⁷ thus far or haven't been tasked with computational problems yet⁴.

Multiple nuclear spin qubits in diamond, on the other hand, can be efficiently controlled by a single nitrogen-vacancy (NV) electron spin. Recent progress has positioned nuclear spin registers among the leading platforms^{8,9}, with achieved fidelities of 99.94¹⁰ % and 99.93¹⁰ % for single-qubit and two-qubit gates, respectively. Such experiments have demonstrated diamond quantum registers up to a size of 10 nuclear spins^{11,12}. The reduced number of control lines of these systems and their capability to operate under ambient conditions simplifies the required classical control electronics. This advantage could allow for an increase in qubit count while maintaining high quality gates. However, scaling up the register size in diamond with a single NV is restricted by the limited range of the nuclear dipolar interaction and spectral crowding, making diamond a challenging

candidate for building quantum processors of a size required for operating algorithms on error-corrected logical qubits.

To overcome the scaling limitations of the diamond platform, it is appealing to connect multiple nuclear spin registers by coupling their NVs via the longer range electron dipolar coupling. A central capability for such a quantum interconnection, NV-NV entanglement inside of a diamond, has already been achieved but with a limited fidelity¹³. Improved performance is possible with numerically optimized, optimal control microwave pulses¹⁴. While state-to-state sequences are typically straightforward to implement, optimizing the experimental fidelity of a universal gate set for arbitrary input states can present a significant challenge^{15,16}. Furthermore, matching the simulated spin dynamics under optimal control pulses to real systems or transferring pulses between different experiments is often impeded by the individual, non-linear microwave response of each experimental setup.

In this work, we apply a different approach for fidelity improvement. Our method seeks to fundamentally understand the physical sources of infidelity. To this end, we start with a relatively simple gate and analyze how errors affect its dynamics via a combination of experimental and simulation data. Modelling the physics of the full system of four spins (two electron + two nuclear spins) enables us to quantify gate error sources that determine the entangling gate fidelity. This can then be used to identify design principles which mitigate physical error sources in a targeted manner. As a consequence, we can apply simple, analytically defined, sine-envelope^{17,18} microwave pulses while optimizing salient parameters in the design space of the entangling gate which directly contribute to gate infidelity. A further benefit of this method is that these design principles can be generalized to other experiments with similar quantum register geometries.

To demonstrate the effectiveness of our approach, we use randomized benchmarking to measure two-qubit gate fidelities in an electron spin quantum register in ambient conditions. Importantly, our method reaches high fidelity control (two-qubit gate fidelity $F_{2q} = (96.0 \pm 2.5) \%$), outperforming the reported Bell state fidelities in the literature¹⁴ – even without the previously needed optimal control pulses.

As a result and after deriving optimal parameters, our gate operates close to the T_2 decoherence limit of two solid state electron spin qubits and we identify the remaining coherent errors. For diamond quantum computing hardware beyond the noisy intermediate-scale quantum era (NISQ¹⁹), the goal of future experiments will be to surpass the error correction threshold. Our model projects that this is an attainable task at room temperature experimental settings and identifies the physical mechanisms that promise the largest enhancements in fidelity. The prolonged electron coherence time (up to $T_2 \sim 1\text{s}^{20}$) at cryogenic temperature could further improve NV-NV gate fidelity.

Results and Discussion

Diamond quantum register

The quantum register, on which we operate our gate, is fabricated by implanting $C_5N_4H_n$ molecules from an adenine ion source²¹ into a ^{12}C enriched, epitaxially grown diamond layer (see Fig. 1a and details in Methods section). Occasionally, two of the four nitrogen atoms in the molecule end up in close proximity (~ 10 nm) in the diamond lattice and form two negatively charged nitrogen vacancy (NV) centers. NV⁻ initialization and readout are achieved optically: We initialize the spin state with a green laser pulse. If required, the charge state is probed by a weak orange laser pulse exciting only the negative charge state of the NV center²². At room temperature, state-of-the-art readout is only possible by monitoring the total fluorescence from both qubits upon green laser illumination. This approach yields a readout signal proportional to the summed qubit populations, but lacks any information about correlations between them¹³. Note that the NVs are too close to be spatially optically resolvable. Furthermore, the optical absorption is phonon-broadened, precluding selective spectral addressing by excitation in the zero-phonon line. We discuss in the Methods section the measurement operator that relates the observed fluorescence, to the expectation value $\langle \sigma_z \rangle_{NV1+2}$. Each member of our NV pair has a different orientation in the crystal lattice. This results in magnetic spin sublevels of different energies when we apply a magnetic bias field, e.g., $|B_0| \sim 100$ G (Suppl. Note 1), of appropriate orientation. Consequently, in a continuous-wave optically detected magnetic resonance (ODMR) experiment, we observe four lines; two below and two above the zero-field splitting energy (Fig. 1b). We define our qubit subspace by the choice of microwave transitions shown in the inset of Fig. 1b. The separation in the microwave frequency domain allows the implementation of single qubit rotations by

applying pulses with frequencies that match the resonance lines of the respective qubit.

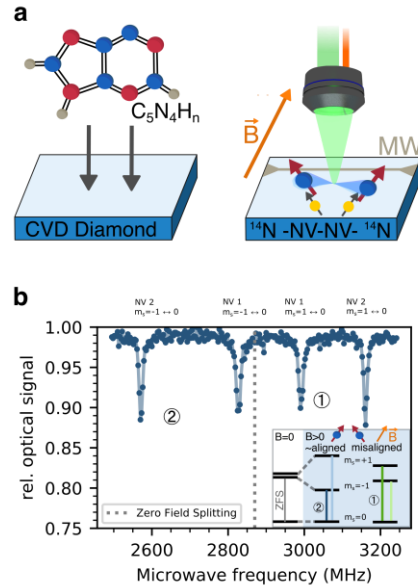


Figure 1. Diamond quantum register. (a) Left: The register is fabricated by implanting adenine molecules into an epitaxially-grown diamond layer. Right: The coupled NV system (consisting of two NV centers plus their inherent ^{14}N nuclear spins) is accessed optically with a confocal microscope. Spin states under a bias magnetic field B are manipulated through a microwave antenna. (b) Optically detected magnetic resonance spectrum of the register in (a). We employ the marked transitions 1 and 2 as “target qubit” and “control qubit”. In principle, these labels are interchangeable. Inset: Sketched energy diagram of a single NV without and with (blue background) magnetic field applied. Here, the control qubit is better aligned with the magnetic field and thus shows a higher splitting in the microwave domain.

Note that the ODMR experiment is not sufficient to reveal a dipolar coupling between the NVs. However, we can detect the presence of a magnetic dipolar interaction of $\nu_{dip} \sim 0.1$ MHz between them with a Double Electron Electron Resonance²³ (DEER) experiment. As the coupling is smaller than the reciprocal dephasing time $1/T_2^* \sim 0.5$ MHz, the entangling gate needs to be embedded into a decoherence-protecting dynamical decoupling pulse sequence. Extending upon previous work¹³, we employ

a two-qubit gate that applies robust XY8 microwave pulse sequences²⁴ on both NVs (see Fig. 2a). Tuning the spin flip time, τ_2 , which is the time interval between the center of the π pulses on the second NV and the time when the first NV is refocused, we can partially refocus the dipolar interaction, adjusting the effective interaction time and acquired phase. Equipped with single-qubit rotations and an entangling operation, we have a gate set that in principle allows for arbitrary two-qubit quantum computations²⁵. In the following, we characterize our gate fidelity using randomized benchmarking and a repetitive benchmarking approach²⁶. Next, we discuss the influence of the five most prominent error sources in the quantum register: Imperfect charge state initialization, microwave crosstalk and leakage, coupling to the inherent ^{14}N nitrogen spin and an off-axis magnetic field component.

Entangling gate

First, we establish the quantum unitary evolution operation of our entangling gate, which we call the \sqrt{ZZ} gate, in the basis of the computational basis states $\{|00\rangle, |01\rangle, |10\rangle, |11\rangle\}$ and up to a global phase, to be:

$$U_{\sqrt{ZZ}} = \text{diag}(1, i, i, 1). \quad (1)$$

While this unitary is analytically derived in Suppl. Note 4 from the gate's microwave sequence in Fig. 2a, a more intuitive understanding can be gained by observing the spin evolution on the Bloch sphere equator. To this end, we bring the first NV ("target qubit") into a superposition state and apply our \sqrt{ZZ} gate sequence. Choosing such an input state to our gate renders the experiment a dynamically decoupled DEER²⁷ and varying the spin flip time τ_2 allows us to measure the dipolar coupling. The DC signal field created by the magnetic moment of NV 2, the "control qubit", is toggled by π pulses with the same repetition rate as the dynamical decoupling of the target qubit. In this way,

low frequency noise is suppressed on both spins and the resulting unitary is

$$U(t_{evol}) = \text{diag}(1, e^{igt_{evol}}, e^{igt_{evol}}, 1) \quad (2)$$

where $g = 2\pi\nu_{dip}$ is the dipolar coupling (in angular frequency units) and $t_{evol} = N_\pi\tau_2$ is the effective evolution time with N_π being the total number of π pulses on each NV (see Suppl. Note 4).

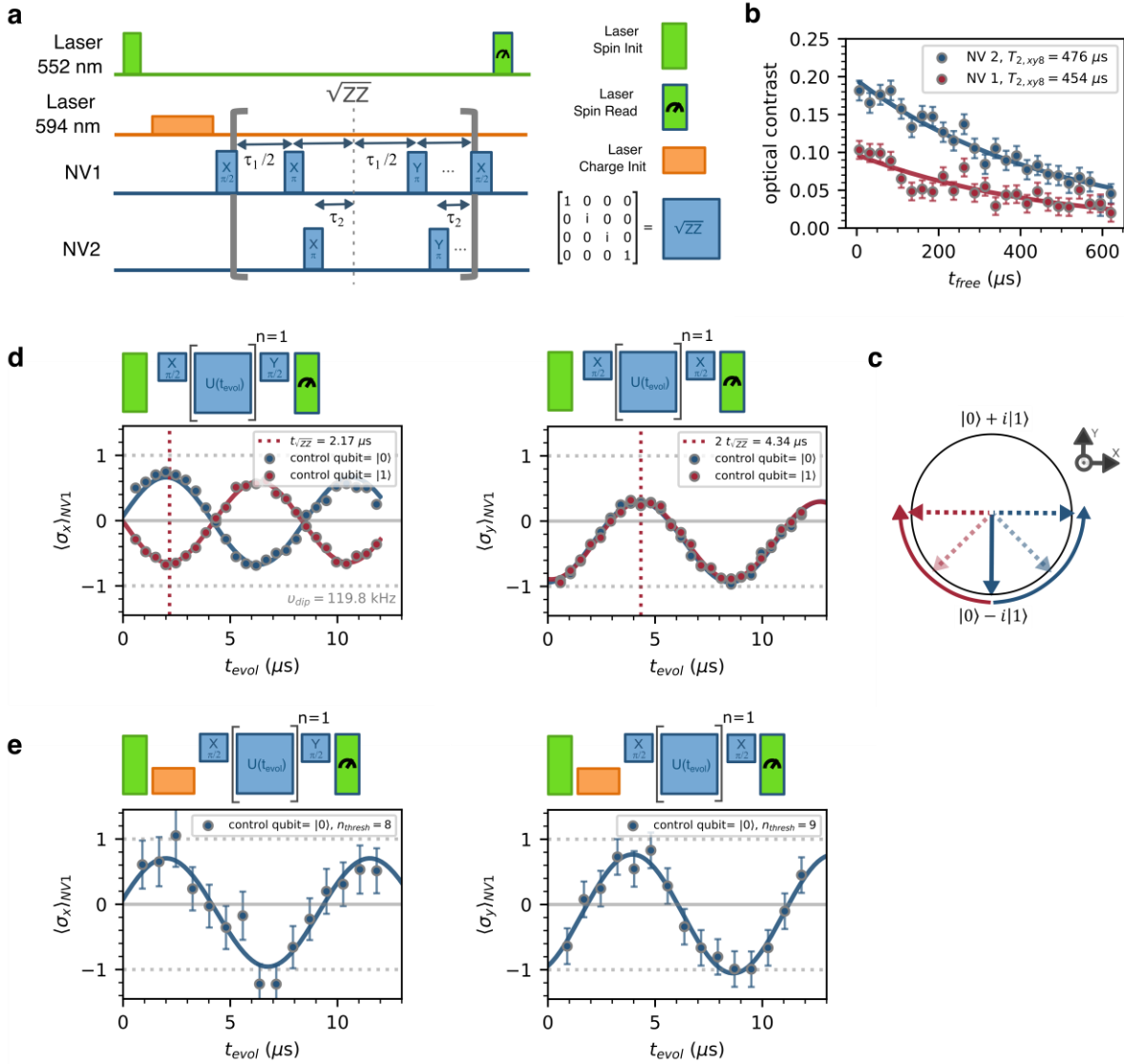


Figure 2. Entangling gate. **(a)** Microwave and laser sequence for probing the \sqrt{ZZ} entangling gate. Blue: Envelope-shaped microwave pulses resonant with NV 1 (target qubit) and NV 2 (control qubit) of labeled phase (X or Y) and pulse area ($\pi/2$ or π). For each NV, $N_\pi = 8$ (phase cycled with XY8-1) π pulses inside the grey brackets form the \sqrt{ZZ} gate. For the sake of a clear figure, only two of the eight pulses per NV are drawn. The $\pi/2$ pulses around the gate are used to initialize the target qubit to the Bloch sphere equator and map the evolution under the gate onto the σ_z readout axis. Green: $3 \mu s$ pulses of the 552 nm laser used for spin initialization and readout (blue stroke). Orange: 3.5 ms pulses of the the 594 nm laser for optional charge state initialization. The unitary matrix on the right is realized for a calibrated $\tau_1 = 800 \text{ ns}$, $\tau_2 = t_{\sqrt{ZZ}}/N_\pi$, $n = 1$. **(b)** T_2 coherence measurements for both NVs by applying a XY8- n sequence with fixed pulse spacing $\tau_1 = 800 \text{ ns}$ sequence and varying order n_{xy} (total sequence duration $t_{free} = 8n_{xy}\tau_1$) to only one of the NVs, respectively. **(c)** Idealized spin dynamic under the gate with initial $\pi/2$ pulse as in (d) on the Bloch sphere equator of the target qubit for the cases control qubit state = $|0\rangle/|1\rangle$ (blue/red). A control qubit conditioned rotation from $\tau_2 = 0$ with no acquired phase evolves for $\tau_2 > 0$. **(d)&(e)** Measured evolution of the σ_x , σ_y component of the target qubit for varying τ_2 in the \sqrt{ZZ} gate sequence ($t_{evol} = N_\pi n \tau_2$, here $\tau_1 = 3000 \text{ ns}$, $n = 1$, $N_\pi = 8$; fitted with $y = A_s \sin(2\pi\nu_{dip} t + \phi_s) + y_{0,s}$, where $A_s, \phi_s, y_{0,s}$ are free parameters). The \sqrt{ZZ} gate is realized after $t_{\sqrt{ZZ}}$. The target qubit is initialized and mapped onto σ_z as given by the respective microwave sequence. Charge initialization with threshold parameter $n_{thresh} = 8, 9$ is applied for (e).

In our example, the target qubit is initially in a coherent superposition state, so it collects a phase from the coupling to the control qubit that is initialized into $|0\rangle/|1\rangle$. For the special case of π pulses on the control qubit that are centered with respect to the π pulses on the target ($\tau_2 = 0$), the signs of the collected phases cancel and ideally the target qubit undergoes no phase evolution in total. The accumulated phase within a decoupling sequence can thus be calibrated by a careful choice of $t_{evol} = N_\pi \tau_2$ ($-\tau_1/2 \leq \tau_2 \leq \tau_1/2$). The evolution on the Bloch sphere equator is revealed by applying a projection $\pi_x/2$ or $\pi_y/2$ pulse that maps the σ_y and σ_x component of the state vector onto the σ_z read-out axis. In the experiments (Fig. 2d), we observe the behavior sketched in Fig. 2c: In the σ_x component, a sinusoidal evolution arises as more phase is acquired through the dipolar interaction by a longer τ_2 . We extract the dipolar coupling $v_{dip} = (119.8 \pm 1.0)$ kHz between the two NVs from the fitted sine oscillation frequency. This value sets an upper limit of (9.54 ± 0.03) nm on the distance between the NV centers²⁸. An exact distance estimate would require knowledge the relative orientation of the dipoles and could be obtained by repeated DEER measurements in a varying bias magnetic field²⁹. The \sqrt{ZZ} unitary in Equation 1 is realized after a quarter rotation on the target qubit's Bloch sphere equator. We thus find a calibrated evolution time $t_{\sqrt{ZZ}} = N_\pi \tau_{2,\sqrt{ZZ}} = (2.17 \pm 0.02)$ μ s and describe details of the gate calibration and the optimization of the π pulse spacing $\tau_1 = 800$ ns in Suppl. Note 4. When calibrating, care must be taken to minimize unwanted population transfer to the inherent ^{14}N nuclear spins that can occur due to the misaligned magnetic field to the NV axes. Furthermore, we demonstrate the controlled nature of the gate that is required for a computationally complete gate set. Flipping the

control qubit to $|1\rangle$ reverses the direction of the DEER oscillation. Consequently, in this case the sign of the σ_x component is opposite in Fig. 2d. As expected, the σ_y component stays constant on flipping of the control qubit.

Comparing the minimal gate time $1/(2v_{dip}) = 4.2$ μ s to the coherence times $T_{2,XY8} = (454 \pm 58)$ μ s, (476 ± 30) μ s for each NV measured in Fig. 2b, we anticipate high quality entangling operations. In these T_2 measurements, we keep the pulse spacing τ_1 constant and increase the number of decoupling π pulses, which naturally compares to repeated application of our gate sequence that uses fixed τ_1, τ_2 .

An important aspect of the gate performance is found in the sine oscillation amplitude and offset parameters. Ideally, we expect a circular-like oscillation on the Bloch sphere equator corresponding to a sine amplitude of one and zero offset. The apparent deviations from this behavior in Fig. 2d can be explained by the imperfect initialization of the NV charge state. If any of the NVs is neutrally charged (NV^0), no ZZ phase is collected during the \sqrt{ZZ} gate ($g = 0$); the output state is independent of τ_2 and thus generally far off the target state. Applying a green (552 nm) laser pulse yields a steady state charge distribution of ~ 0.7 NV^- and ~ 0.3 NV^0 for a single NV³⁰. Neglecting any collective charge influences, statistics yields only a probability of $p(\text{NV}^-, \text{NV}^-) = 0.49$ for both NVs to be in the desired negative charge state. In total, the observed oscillation is an average over the different charge cases. On the one hand this lowers the contrast of both the σ_x, σ_y oscillation, as seen in Fig. 2c. Second, the σ_y component becomes asymmetric (offset parameter of fitted sine $y_{0,s} < 0$), as this component stays $\langle \sigma_y \rangle_{\text{NV}1} = -1$ for all τ_2 given a wrong charge state and the degree of asymmetry ($|y_{0,s}|/A_s$) can be a direct measure of the charge state of the NV pair (Suppl. Note 5).

In Fig. 2e, we mitigate the charge initialization error by using a weak orange laser charge initialization technique²². While fast-feedback pre-selection has been demonstrated as a time-efficient mean to reach high NV⁻ charge purity³¹, we here employ less demanding post-selection, thresholding (with a parameter n_{thresh}) over data sets containing all detected fluorescence photons. The DEER oscillations in Fig. 2e, show improvements in contrast and asymmetry of the σ_y component. Yet, there remains a significant deviation from full, symmetric contrast. This is in accordance with the limited charge state fidelity $F_{NV-,NV-} = (83 \pm 6) \%$ measured in a separate measurement in Suppl. Fig. 4. There, we also show that the charge state fidelity can be improved by increasing the threshold parameter n_{thresh} of the post-selection. However, stricter thresholding comes at the cost of a worsened signal-to-noise ratio. Nevertheless, higher photon collection efficiency, provided, e.g., by micro structured lenses³² or doping-induced NV charging³³⁻³⁵, could enhance charge state fidelity significantly.

Repetitive benchmarking

Imperfections that are not related to the state evolution during a gate are commonly referred to as state preparation and measurement errors (SPAM)³⁶. We show that the charge state can be treated as a SPAM error. This insight allows to separate between gate and charge state errors and thus to calibrate all gate operations during the “booting” of our diamond quantum register without charge state initialization. Such an approach is compelling, as it enables quick optimization of the gate parameters without the overheads needed to achieve good state preparation. For example, at our experimental

settings, a single charge read laser pulses is ~ 1200 longer than the $3 \mu\text{s}$ green laser pulse for spin readout. After a parameter set for the gates has been found by minimizing the gate errors, the actual quantum computation could take place with charge state-initialization. Beyond a certain problem size, the exponential speedup expected from quantum algorithms could then outweigh the slow readout rate that room temperature, charge initialized diamond quantum processors would currently provide.

We use repetitive benchmarking, i.e. repeated application of the gate to a certain input state²⁶, to separate the entangling gate fidelity from SPAM errors. We demonstrate that this tool quantifies gate errors independently of the charge state. This is achieved by repeated application of the gate under test. After a certain repetition number n , single qubit rotations are applied to reverse to the ground state and the $\langle \sigma_z \rangle$ expectation value is measured. In the resulting decay curves, errors occurring during the gate operation are collected in the lifetime parameter of a fitted model which we convert to a pseudo error per gate (pEPG) metric (see Methods). We note that the pEPG derived here from the lifetime parameter of an exponential fit is a useful tool for easily implementable benchmarking, but the results are difficult to compare among experiments (which motivates our labeling as “pseudo” EPG). We empirically find a single exponential decay, which is also the decay model widely used in T_2 measurements³⁷. While repetitive benchmarking is similar to T_2 experiments - except for the additional evolution by the dipolar coupling - the exact nature of the decay depends on the environment of the probed spins^{38,39}.

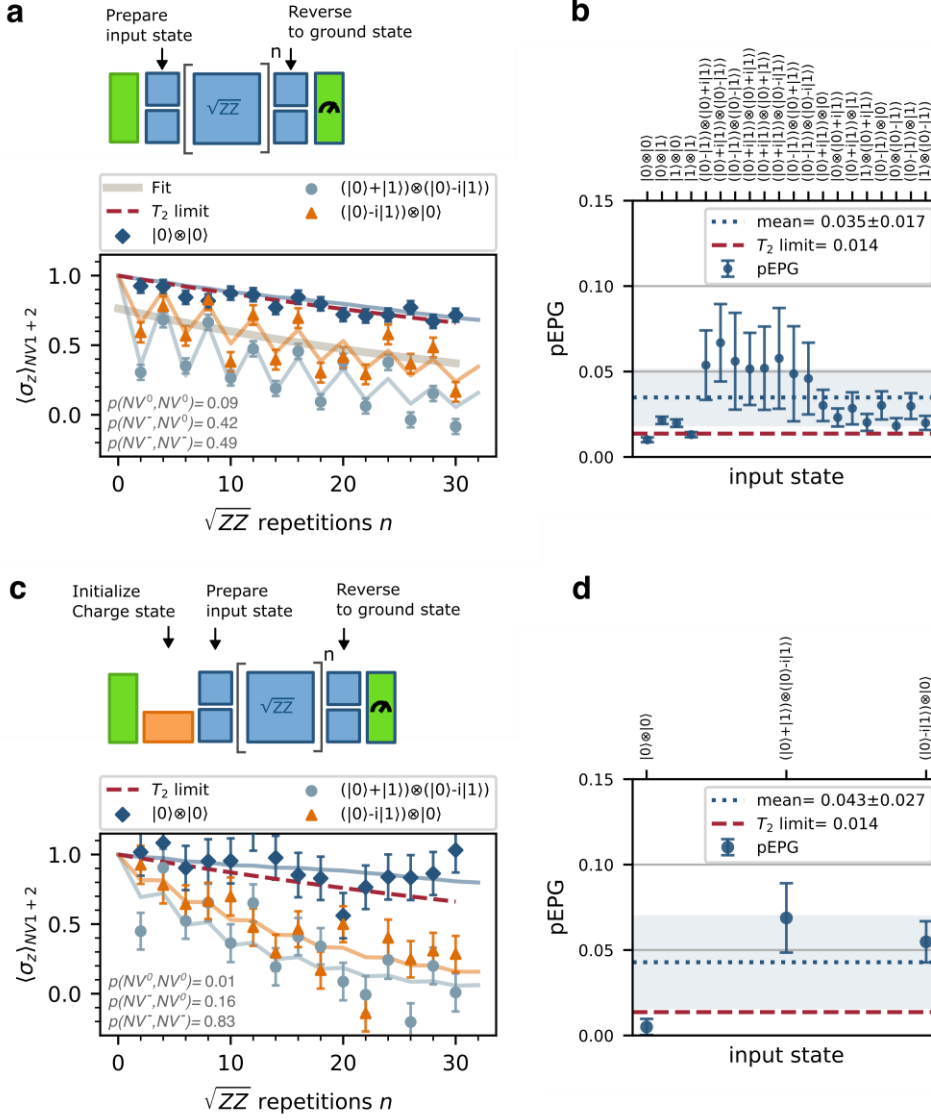


Figure 3. Repetitive benchmarking. **(a)&(c)** Measured surviving population after n applications of the \sqrt{ZZ} gate. For each data point, a reverse circuit is added that returns to $|00\rangle$ in the absence of gate and preparation errors. Data for exemplary input states, an exponential fit (grey line) to extract the pEPG for input state $(|0\rangle - i|1\rangle)\otimes|0\rangle$ and simulation results including the charge state behavior are shown (colored solid lines, charge state probabilities annotated). **(b)&(d)** Extracted pEPG from the data in (a)&(c) for all probed input states. The charge state induced modulation in the decay data described in the main text leads to the plotted 1σ fit errors that depend on the input state. Blue shading represents the standard deviation of all data points. Charge initialization is applied for (c)&(d). Mean is calculated as average over the mean pEPGs of each input state group to ensure comparability between (b)&(d).

In Fig. 3a, we show decays on repetitive application of the \sqrt{ZZ} gate for three exemplary input states. As a benchmarking result, we find a mean $\overline{pEPG} = 0.035 \pm 0.017$ averaged over all tested input states (shown in Fig. 3b), which corresponds to a pseudo gate fidelity of

$pF_{2q} = 1 - \overline{pEPG} = (96.5 \pm 1.7) \%$. This value is only a factor of 2.5 away from the T_2 limit $pEPG_{T_2} = 0.014$ that we calculate from the in an independent coherence measurement (Fig. 2b). We conclude that coherent gate errors

are qualitatively small and will later quantify the different contributions.

The input states can be grouped into three classes of pEPGs: The computational basis input states show the lowest gate errors as they're less susceptible to magnetic noise. Bringing one of the qubits into superposition increases the gate error. With such a superposition input state, magnetic noise shifting the qubit's resonance frequency faster than the dynamical decoupling frequency $1/\tau_1$ causes decoherence during the gate operation. Finally, input states with both qubits in superposition yield entangled states during the gate evolution for gate repetitions n with $\text{mod}(n,2)=1$. Thus, not only both qubits will couple to the magnetic noise decoherence channel, but also some entangled states will pick up this noise more efficiently⁴⁰.

A prominent feature in repetitive benchmarking is an additional modulation with a period of four that occurs for input states that are not the computational basis states. This behavior is a consequence of the charge state SPAM error and can be understood, e.g., for the input state $(|0\rangle - i|1\rangle) \otimes |0\rangle$ (simplifying notation, this abbreviates $|\Psi\rangle_{NV1} \otimes |\Psi\rangle_{NV2} = \frac{|0\rangle - i|1\rangle}{\sqrt{2}} \otimes |0\rangle$ with dropped normalization throughout this work). For $\text{mod}(n,4)=2$, half a rotation has taken place on the Bloch sphere equator of the target qubit. When both NVs are initialized as NV⁻, the accumulated phase is $gt_{evol} \approx n\pi/2$ and $U(t_{evol}) = \text{diag}(1, -1, -1, 1)$ for $\text{mod}(n,4)=2$. However, when one of them is initialized as NV⁰, the coupling is $v_{dip} = 0$ and $U(t_{evol})$ is the identity operator (up to an irrelevant global phase). This SPAM error has no effect when the initial state is a computational basis state as the latter is not affected by $U(t_{evol})$, independent of the charge state. However, imperfect initialization reduces the output state fidelity when any of the NVs is in a superposition state with double

superposition states showing the greatest error (see Fig. 3a). This is also shown in Fig. 2d, where a low charge state initialization fidelity causes asymmetry in the σ_y component of the DEER oscillation and thus a reduced contrast in the repetitive benchmarking. Data points satisfying $\text{mod}(n,4)=0$, however, show nearly no influence from the charge state as $U(t_{evol})$ is ideally the identity operator with and without a SPAM error. Specifically, for such data points, the output state after integer rotations on the Bloch sphere equator is equal to no conditional evolution at all; just like it is the case if the control qubit is in the wrong charge state. We simulate the repetitive benchmarking experiment in Fig. 3a&c considering all charge state configurations (details in Method section). The experimentally observed dependence of the modulation depth on the chosen input state is well reproduced.

When adding charge state initialization to the repetitive benchmarking in Fig. 3c, the modulation is reduced and we extract a slightly elevated $\overline{pEPG} = 0.043 \pm 0.027$. Comparing this mean \overline{pEPG} for the charge-initialized case in Fig. 3d with the steady state initialized data in Fig. 3b, we find agreement within the standard deviation calculated from the data of all input states. The statistically not relevant increase in pEPG could be explained by the longer measurement time required for charge-initialization that makes the experiment more susceptible to long term environmental drifts. We conclude that repetitive benchmarking allows to measure gate errors separately from the charge initialization error. The latter SPAM error can be significantly reduced by charge state mitigation strategies, as described in the previous section.

Randomized benchmarking

Randomized benchmarking³⁶ has emerged as a standard tool to evaluate gate performance. It can be measured time-efficiently and yields a

fidelity metric of an average computation with a priori limited insight into the nature of the gate error. To gain a fidelity measure that separates gate errors from SPAM and additionally is comparable to different quantum hardware

platforms and errors, we perform two-qubit randomized benchmarking in Fig. 4a&b. (Implementation details are presented in the Methods section.)

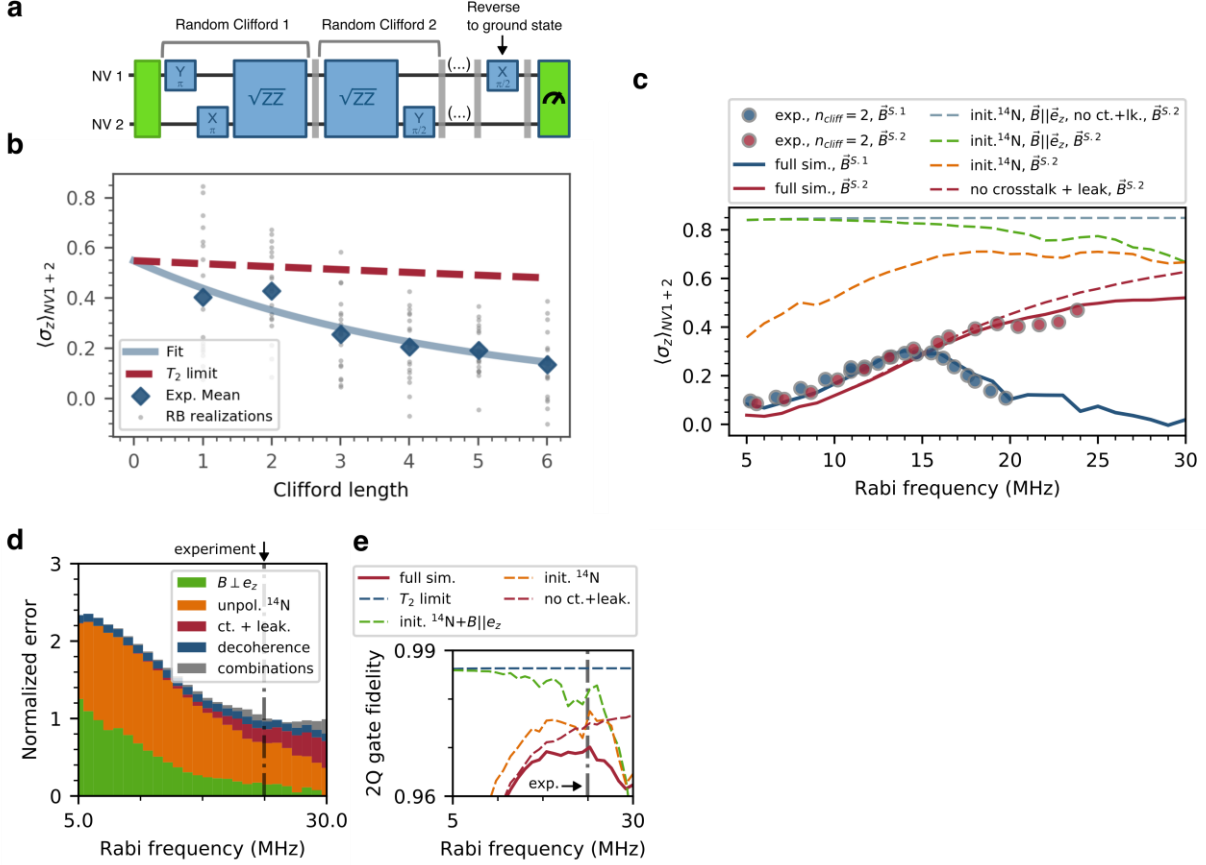


Figure 4. Randomized benchmarking and gate error analysis. **(a)** Sketched gate sequence for a single randomized benchmarking data point. Random Clifford gates are generated and reversed to the ground state. **(b)** Surviving population after randomized benchmarking in our optimized experimental setting (magnetic field setting 2, $\Omega_{rabi}/(2\pi) = 23.7$ MHz, 20 random experiments per Clifford length). From a single exponential fit, the EPC of the gate set discussed in the main text is extracted. **(c)** Randomized benchmarking at a fixed Clifford length $n_{cliff} = 2$ for varying Rabi frequencies ($\Omega_{rabi} = \frac{\pi}{t_\pi}$ with approx. same duration t_π of sine envelope-shaped π pulses for both NVs). Each data point is a mean of 20 random experiments. The solid blue (red) line is a simulation at magnetic field setting 1, ~ 60 G (magnetic field setting 2, ~ 100 G), which contains a free parameter to account for the experimental SPAM errors (see Methods section). From the dashed lines, which are simulations at magnetic field 2 where the labeled error sources, i.e. crosstalk + leakage, unpolarized ^{14}N spin, magnetic field orthogonal to the orientations of the NVs e_z , are turned off, we extract the relative error contributions in (d). **(d)** Error contributions to the gate set for varying Rabi frequencies, normalized to the error at the experimental $\Omega_{rabi}/(2\pi) = 23.7$ MHz, magnetic field 2. The attribution to the labeled error sources is presented in the Methods section. **(e)** Simulated gate fidelity of the \sqrt{ZZ} gate including a decoherent contribution multiplied to the decoherence-free simulation ($EPG_{T_2} = 1.4\%$ from measured T_2 coherences, Methods).

In our optimized setting (magnetic field 2 in Suppl. Table 1 is used in this work if not stated otherwise, $\Omega_{rabi}/(2\pi) = 23.7$ MHz) we find a fidelity for our entangling gate of $F_{2q} = (96.0 \pm 2.5) \%$ as extracted from an error per two-qubit Clifford gate $EPC = (14.9 \pm 2.7) \%$ and pre-characterized average effective single-qubit errors of $F_{1q} = (99.23 \pm 0.12) \%$ (see Equation 10, Suppl. Note 3). Our entangling gate fidelity, even though reflecting errors for arbitrary input states, is better than the best reported NV-NV entangled state fidelity ($82.4 \%^{14}$) that was optimized by state-to-state transfer optimal control algorithms. We emphasize that the improved performance takes into account errors for arbitrary input states, in contrast to a state-to-state transfer fidelity. As we perform our measurement without an initialized charge state, the measured SPAM error, represented in the amplitude parameter of the fitted exponential decay, is large. Interestingly, the decay's lifetime in Fig. 4b is shorter than expected from repetitive benchmarking (factor $EPC/EPC_{T2} = 5.9 \pm 1.1$, $\overline{pEPG}/pEPG_{T2} = 2.5 \pm 1.2$, coherence limit EPC_{T2} derived in Methods section) and substantially shorter than if only decoherence was limiting the experiment. We attribute this to the fact that other, coherent errors sources are dominating the probed gate set. In repetitive benchmarking, those errors are well refocused by the symmetric timing of the decoupling π pulses in the \sqrt{ZZ} gate sequence. In combination with random single-qubit Clifford gates in randomized benchmarking, this decoupling works less efficient.

Gate error sources

Apart from decoherence, we show that three error sources (sketched in Suppl. Fig. 6a) mainly limit our gate fidelity: As the inherent ^{14}N spins of both NVs are unpolarized, the nuclear spin state is random at the beginning of every experimental shot. Consequently, most of

the microwave pulses suffer from a detuning $\Delta = \pm A_{zz}/(2\pi) = \pm 2.16$ MHz from the correct microwave transition frequency for the electron, if the nitrogen state is $m_I = \pm 1$. Additionally, the unpolarized nitrogen spin causes free evolution on the non-addressed NV in our single qubit gate implementation (that we discuss in Suppl. Note 3). Second, all microwave pulses generate a small, unwanted microwave drive on the other NV ("crosstalk") or transitions to states out of the qubit subspaces ("leakage"). In a simple picture, this happens as any pulse has a finite width in the spectral domain and thus can overlap with other transitions. Last, in a magnetic field setting that is aligned to the NV quantization axis, the diagonal hyperfine interaction tensor $\underline{A} = \sum_{i=x,y,z} A_{ii} S_i \otimes I_i$ in the Hamiltonian (see Methods, Suppl. Note 2) effectively only contains $S_z \otimes I_z$ terms. Here, S_i, I_j denote the $S = I = 1$ spin operator of the NV and the ^{14}N spin, respectively. In our geometry however, magnetic field misalignment is unavoidable and in the tilted basis the hyperfine tensor is no longer diagonal. Then, terms of, e.g., the form $S_z \otimes I_x$ appear and can cause population transfer from the qubit to the nitrogen spin.

We measure the influence of the different error sources by performing two-qubit randomized benchmarking while varying the Rabi frequency of all pulses of the gate set. In order to keep the measurement time viable, we determine only the surviving population $\langle \sigma_z \rangle_{NV1+2}$ for a fixed Clifford length $n_{cliff} = 2$. This allows us to extract relative error contributions, as described in the Methods section, but yields no absolute gate error metric¹⁵. Two error source regimes are directly observable in Fig. 4c: As expected, low Rabi frequencies deteriorate our gate set fidelity as the hyperfine lines caused by the ^{14}N spin are driven less homogeneously. Increasing the Rabi frequency is only beneficial until microwave crosstalk and leakage become

limiting. For our magnetic field setting 1 (blue line in Fig. 4c, exact parameters in Suppl. Table 1) with modest frequency separation, an optimal Rabi frequency of ~ 15 MHz is observed. We find that a high Rabi frequency can strongly reduce gate errors if we simultaneously mitigate crosstalk to unwanted resonance lines through an increased frequency separation in the higher magnetic field setting (red line) and by employing pulse envelope shaping (here: sine envelope) for all microwave pulses^{17,18}. Consequently, our optimized magnetic field setting 2 (red line in Fig. 4c) features a frequency separation such that even at the highest experimentally accessible drive power, we do not yet see a strong fidelity decrease by the microwave crosstalk or leakage.

However, at higher magnetic field, state mixing for the misaligned NV 1 becomes relevant. For elevated perpendicular magnetic field components, spin initialization by green laser excitation starts to be ineffective and yields a partly mixed spin state. We note that this effect should be treated as a SPAM error, even though the lowered readout contrast will not be visible in a typical NV randomized benchmarking experiment that usually involves a normalization step to convert fluorescence to qubit population. We estimate the SPAM error introduced solely by spin mixing at the higher magnetic field setting to $\sim 17\%$ by Rabi measurements on both spins in Suppl. Fig. 5a. For small NV quantum registers, such a SPAM error by spin mixing seems acceptable, especially when a higher gate fidelity can be reached in turn. On the other hand, larger scale quantum processors will require to mitigate state mixing, as state preparation errors are only inefficiently correctable⁴¹.

We employ a model (Methods section) that accurately describes the experimental randomized benchmarking results to quantify the influence of different gate error sources. In Fig. 4c, the experimental data at Clifford length

$n_{cliff} = 2$ is well reproduced by our simulation for both magnetic field settings. Turning off one error source at a time, we can extract the relative error contributions to our gate set at our optimized setting in Fig. 4d. For low Rabi frequencies the absolute gate errors are large and roughly equally explained by the unpolarized nitrogen ^{14}N in combination with the misaligned magnetic field. Towards higher Rabi frequencies the relative contribution of the latter decreases but crosstalk and leakage become significant. At the experimentally chosen Rabi frequency $\Omega_{rabi}/(2\pi) = 23.7$ MHz, the biggest single error contribution of 53 % is the unpolarized nitrogen ^{14}N spin. The misaligned magnetic field makes up for 15 % of the observed error in the simulation. Crosstalk and leakage contribute to 18 % of the error, which demonstrates the efficacy of our pulse envelope shaping. Some part of the gate infidelity cannot be attributed to a single error. This cumulative effect increases in parallel with crosstalk and leakage but has a small contribution (4 %) at the experimental setting. In the Methods section we discuss in more detail how we estimate the remaining errors, for instance dipolar evolution during microwave pulses, to be $<1\%$ in our experiment. We note that all coherent error sources investigated in Fig. 4 could be corrected with appropriate correction sequences. The relative decoherent contribution estimated from $T_{2,XY8} = 454 \mu\text{s}$, $476 \mu\text{s}$ per qubit is 10 %.

Finally, we can project the achievable gate fidelities from our model under a realistic scenario for future experiments in Fig. 4e. While before, we discussed how gate errors affect the fidelity of the gate set as measured in randomized benchmarking, our model also allows direct determination of the entangling gate fidelity (97.0 % at our settings, incl. decoherence). We observe that optimized microwave pulses with no crosstalk or leakage would only barely improve the entangling gate fidelity to 97.5 % in a geometry with NVs of

different orientation. Polarizing the nuclear spin yields a similar gate fidelity improvement. As they are not protected by dynamical decoupling, the influence of the unpolarized nitrogen spin on the single-qubit rotations and the gate set is more pronounced than on the entangling gate (see also all simulated gate fidelities in Suppl. Fig. 6b). A more substantial improvement to 98.2 % is expected with an initialized ^{14}N spin state and aligned magnetic field or by a modified gate microwave sequence that avoids population transfer to the nitrogen spin more strictly. To reach a two-qubit gate fidelity of 99.0 % that supports realistic error correction protocols^{42,43}, we could extend the coherence of the register by higher order dynamical decoupling^{44,45} and would need to address the discussed coherent errors.

Conclusion and Outlook

We have experimentally demonstrated the highest entangling gate fidelity of $F_{2q} = (96.0 \pm 2.5) \%$ between solid state electron spins at room temperature. Our analysis of the gate error sources reveals that 90 % of those errors are coherent and correctable.

The primary gate error sources are the unpolarized nitrogen spin, which could be addressed by one of the existing nitrogen spin polarization techniques⁴⁶⁻⁴⁹, and the misaligned magnetic field that is unavoidable for NV geometries with different orientation in the crystal lattice. A perfectly aligned magnetic

field, albeit technically challenging, would be possible for NV quantum registers of same orientation that are conceivable when applying strong magnetic gradient fields^{50,51} ($\sim 1 \text{ G/nm}$) or leveraging different nitrogen isotopes of each NV. The smaller remaining microwave errors (crosstalk and leakage) could be mitigated by optimal control⁵²⁻⁵⁵.

We found that we incur a non-negligible SPAM error due to spin mixing in the misaligned magnetic field. Operating at cryogenic temperatures ($\sim 4 \text{ K}$) would significantly decrease both of the current initialization errors. First, resonant laser excitation of the sharp optical absorption lines⁵⁶ would enable fast, high fidelity charge state initialization^{57,58}. Additionally, spin mixing errors could be avoided for arbitrary magnetic field geometries, as spin initialization would be possible without cycling through the NV singlet state⁵⁷ and thus independent of the off-axis magnetic field component. Last, narrow optical lines would allow to distinguish the NV photons spectrally and enable to measure spin correlations between the NVs.

Integrating up to four⁵⁹ coherently coupled NV centers each with nuclear spin registers of ~ 25 qubits¹⁰⁻¹² seems realizable with current experimental techniques. Our error analysis suggests that the gate fidelities on such a larger-scale diamond quantum processor could support error-corrected operation.

Methods

Sample

The sample used in this study is a type IIa (100) single-crystalline diamond film that is homoepitaxially grown on a high-pressure high-temperature type Ib substrate via microwave-plasma-assisted CVD⁶⁰. The CVD film thickness is 20 μm . To suppress the effects of ^{13}C on the coherence properties of the NV centers, a ^{12}C -enriched (99.95 %) high-purity (nitrogen concentration <1 ppb) diamond is used. The ion implantation process of this sample was already described elsewhere²¹. Ionized $\text{C}_5\text{N}_4\text{H}_n$ ions are extracted from adenine powder and accelerated to 65 keV kinetic energy. The implantation fluence of 10^8 is achieved after 10 s. After ion implantation, the sample is annealed at 1000 $^\circ\text{C}$ for 2 h in a forming gas (4 % H_2 in Ar) to create NV centers and recover the diamond lattice. The sample is annealed in an oxygen environment at 465 $^\circ\text{C}$ for 4 h, followed by cleaning in a 1:1:1 mixture of HNO_3 , H_2SO_4 , HClO_4 at 200 $^\circ\text{C}$ under a pressure of 6-8 bar for 30 min.

For the NV pair used as a quantum register, we measured a dephasing (Ramsey) and decoherence (Hahn echo, XY8) times

of $T_2^* = (2.60 \pm 0.11) \mu\text{s}$; $(2.37 \pm 0.13) \mu\text{s}$, $T_{2,HE} = (27 \pm 5) \mu\text{s}$; $(75 \pm 4) \mu\text{s}$, $T_{2,XY8} = (454 \pm 58) \mu\text{s}$; $(476 \pm 30) \mu\text{s}$ on NV 1 and NV 2, respectively.

Setup

We control and read the NV's spin and charge state with a standard home-built confocal microscope. Spin initialization & readout laser pulses of 3000 ns at a wavelength of 552 nm (green) are generated by a cw. laser and an acousto-optic modulator (AOM). The orange (594 nm) charge initialization pulses from a different, digitally modulated cw. laser are 3.5 ms long and of circular polarization to ensure equal ionization rates for both NVs during the charge initialization. The polarization of the green laser is linear and adjusted for near equal readout contrast for data in Fig. 3 and contrasts as listed in Suppl. Table 1 for data in Fig. 2&4.

All laser pulse shapes and microwave waveforms are sampled on an AWG (Keysight M8195A) amplified and applied to the NV through a copper wire of 20 μm diameter placed on top of the diamond. Photoluminescence photons of the NV in the > 680 nm band are collected through an oil-immersion objective lens (Olympus, 60x, NA 1.35), counted by an avalanche photodiode (APD Excelitas SPCM) during a 330 ns gating window at the beginning of the spin readout pulse⁶¹ and digitized by a counting card (FAST ComTec MCS6). The experiment is controlled by a custom measurement software (qudi⁶²) that features a software interface to quantum algorithms generated by Qiskit⁶³.

To convert experimentally measured fluorescence to polarization $\langle \sigma_z \rangle_{NV1+2}$, we perform every experiment twice with additional π pulses on both NVs. The difference Δ_{alt} of such alternating experiments is then normalized to the optical contrast $I_{|00\rangle} - I_{|11\rangle}$ between the fluorescence in state $|00\rangle$ and $|11\rangle$. Our measurement relates to the readout of a register state ρ as $\langle \sigma_z \rangle_{NV1+2} = \Delta_{alt} / (I_{|00\rangle} - I_{|11\rangle}) = R(\rho)$ with the readout outcome R as defined in Suppl. Note 2.¹³

Simulations

For the simulation results of Fig. 4, we use the following Hamiltonian to describe the system of two NV centers in their orbital ground-state 3A_2 :

$$H(t) = H_{NV1}^0 + H_{NV2}^0 + H_{12}^{\text{int}} + H^{\text{mw}}(t) \quad (3)$$

where H_{NV1}^0 and H_{NV2}^0 are the single NV-Hamiltonians, H_{12}^{int} the dipole-dipole coupling Hamiltonian and H^{mw} the microwave Hamiltonian, that is in general time dependent. The single NV center Hamiltonians⁶⁴

$$H^0 = DS_z^2 + \vec{\omega}_e \cdot \vec{S} - QI_z^2 + \vec{\omega}_n \cdot \vec{I} - \vec{S}\underline{A}\vec{I} \quad (4)$$

with $\vec{\omega}_{e/n} \equiv -\gamma_{e/n}\vec{B}$

contain the electron zero-field splitting D , the nuclear quadrupole moment Q , the Zeeman splitting due to the static magnetic field \vec{B}_0 , $\gamma_{e/n}$ the gyromagnetic ratio of the electron/nuclear spin in angular frequency units, and the hyperfine coupling to the ^{14}N

nuclear spin via the tensor \underline{A} . Both the electron spin (initialized in its ground state) and the ^{14}N nucleus (initialized in a maximally mixed state) are triplets: $S = I = 1$. The two NV centers have distinct crystal axes (c.f. Suppl. Fig 1a), causing misalignment between the magnetic field and the NV axes and thus a logical basis that is given by rotated eigenstates.

For simulating the dynamics of the system, we use an effective dipole-dipole interaction (along the quantization axes) in the H_{12}^{int} term that is described in detail in Suppl. Note 2 and list the employed estimates of the system parameters, such as the magnetic field and interaction strength in Suppl. Note 1.

In order to investigate the effect of the charge state initialization SPAM error, we perform a numerical simulation, which takes into account the probabilities that each of the NV centers is initially prepared in either the NV^- , or NV^0 charge state. This simulation employs the simplified Hamiltonian described in Suppl. Note 4 and does not take into account the effect of decoherence. Thus, we include a phenomenological single exponential decay of the observed signal in the charge state simulations in Fig. 3a&c, which is calibrated using the measured pEPGs of Fig. 3b&d.

Repetitive Benchmarking

To convert the measured repetitive benchmarking decays into (pseudo) gate errors, we assume a single exponential decay model that is known to well describe usual $T_{2,XY8}$ measurements on single NVs³⁹. We express the decay in terms of the gate repetition number n as:

$$y = y_0 + a * \exp(-n/N_d) = y_0 + a * p^n \quad (5)$$

where we used the identity $p = \exp\left(-\frac{1}{N_d}\right) = (1 - \text{pEPG})$ to convert the gate decay parameters N_d, p into a gate error pEPG . The remaining free fit parameters are the amplitude a and the offset y_0 .

Similarly, we obtain the T_2 limit decay curve in Fig. 3 by calculating the polarization loss per applied two-qubit gate of length $t_{\text{gate}} = 8\tau_1$ from the mean of the measured $T_{2,XY8}$ of both NVs in Fig. 2b:

$$\text{pEPG}_{T_2} = 1 - \exp\left(-t_{\text{gate}}/(T_{2,XY8,NV1} + T_{2,XY8,NV2})/2\right) \quad (6)$$

Randomized Benchmarking

We use the same single exponential model of Equation 5 to obtain a decay parameter p for the observed randomized benchmarking decays. If the gate-dependency of the errors is small enough, the measured EPC becomes a good estimate of the average gate set infidelity⁶⁵.

$$\text{EPC} = \frac{2^n - 1}{2^n} (1 - p) \approx \frac{\sum_i (1 - F_{\text{avg}}(\tilde{C}_i, C_i))}{\sum_i 1} \quad (7)$$

where n is the number of qubits, $\{\tilde{C}_i\}$ are the Clifford gates and $\{C_i\}$ the respective ideal ones (to account for the possibility of gate-dependent errors⁶⁵), and

$$F_{\text{avg}}(\tilde{C}_i, C_i) = \int d\psi \text{Tr}(\tilde{C}_i[|\psi\rangle\langle\psi|]C_i[|\psi\rangle\langle\psi|]) \quad (8)$$

is the state averaged overlap between the actual process matrix of the i -th Clifford \tilde{C}_i and the ideal C_i . F_{avg} is averaged over all possible initial pure states ψ .

Our experiments are generated from the Qiskit software package using the gate set $\{\pi_x, (\pi/2)_x, \pi_y, (\pi/2)_y, C_1\text{NOT}_2\}$ and 20 random experiments per Clifford. While the single-qubit rotations are easily realized on our NV hardware by microwave pulses with appropriate phases, we need to express $C_1\text{NOT}_2$ in terms of our available \sqrt{ZZ} gate and multiplication with single-qubit unitaries:

$$C_1\text{NOT}_2 = \pi_{x,1} * (\pi/2)_{-y,2} * \sqrt{ZZ} * (\pi/2)_{x,1} * (\pi/2)_{y,2} * (\pi/2)_{y,1} * (\pi/2)_{-x,2} * (\pi/2)_{x,1} \quad (9)$$

After running Qiskit's automatic transpiler optimization ("Optimize1qGatesDecomposition") to reduce the number of single-qubit gates, we end up with a randomized benchmarking experiment that contains on average $GPC_{1q} = 10.5$ single-qubit $(\pi_x, (\pi/2)_x, \pi_y, (\pi/2)_y)$ and $GPC_{2q} = 1.8$ two-qubit (\sqrt{ZZ}) native gates per Clifford gate. The measured EPC could be improved by finding a more efficient gate set with smaller GPC_{1q} .

Two-qubit randomized benchmarking yields an EPC that is an average error over the whole gate set. For estimating the error of our \sqrt{ZZ} gate, we use the EPC definition⁶³:

$$EPC = 1 - \prod_i (1 - EPG_i)^{GPC_i} = 1 - (1 - EPG_{2q})^{GPC_{2q}} (1 - EPG_{1q})^{GPC_{1q}} \quad (10)$$

where we collected all single-qubit gate errors in an average gate error EPG_{1q} . Solving for EPG_{2q} allows us to estimate the two-qubit gate error from the measured two-qubit randomized benchmarking (yielding EPC) and the pre-characterized average effective single-qubit error per Clifford $EPC_{1q} = 1 - (1 - EPG_{1q})^{GPC_{1q}}$ (data in Suppl. Fig. 2).

Our randomized benchmarking uses the single exponential model in Equation 5 as a decay model and yields results with low statistical uncertainty, if the tail of the decay curve is well captured. Due to limitations of the applicable microwave power, this is not always possible in our experiment. For the two-qubit case, we thus determine the offset parameter y_0 of the decay separately first, by applying a high number of intentionally miscalibrated pulses, and fix the decay offset parameter. This amplifies gate errors and thus gives a value that is equally representing the high error limit. We consistently observe $y_0 < 0.001$ in our experiments.

From simulations we find that a single exponential decay with offset $y_0 = 0$ is well describing the behavior for experimentally accessible numbers of two-qubit Clifford gates. For $n_{cliff} \gg 10$, accumulated crosstalk and leakage become more relevant, which can cause a slower, 2nd exponential decay⁶⁶ and depolarization into equal populations of the three $m_s = 0, \pm 1$ sublevels.

Coherence limit

For the T_2 coherence limit in Fig. 4, we first estimate the error caused by decoherence per two-qubit gate assuming the same single exponential decay as in the repetitive benchmarking case, thus $EPG_{T_2,2q} = pEPG_{T_2}$. The decoherence errors from single-qubit gates are much smaller, as they feature shorter gate lengths. Hence, we roughly estimate $EPG_{T_2,1q}$ by inserting the average single-qubit gate length into Equation 6. Knowing the average number of gates per Clifford, we obtain the coherence limit per Clifford EPC_{T_2} from Equation 10.

Relative error contributions

We extract the relative error contribution in randomized benchmarking (Fig. 4d) from the simulation as follows: First, we simulate the $(\sigma_z)_{NV1+2}$ outcome of the experiment at $n_{cliff} = 2$ with all (coherent) error effects and multiply this value (z_{sim}) with the known EPC_{T_2} to account for the decoherence of a single average Clifford gate:

$$z_{sim,T_2} = z_{sim}(1 - EPC_{T_2}) \quad (11)$$

Using the single exponential decay in Equation 5, we convert the simulated outcome of the randomized benchmarking experiment to an average fidelity parameter p :

$$p_{full,T_2} = \sqrt[n_{cliff}]{(z_{sim,T_2} - y_0)/a} \quad (12)$$

where we take the SPAM parameters a, y_0 from the measurement in Fig. 4a.

The deviation of our simulation (in terms of p) including all errors from a perfect, gate error free experiment with $p=1$ is:

$$\begin{aligned} \Delta_{full,T_2} &= 1 - p_{full,T_2} \\ \Delta_{Er,T_2} &= 1 - p_{Er,T_2} \end{aligned} \quad (13)$$

Similarly, we obtain average fidelity parameters p_{Er_i, T_2} for turning off specific error sources Er_i . Then, the relative contribution $c_r(Er_i)$ is given by the difference between full simulation and the improved result without this error source p_{Er_i, T_2} divided by the swing of the full experiment:

$$c_r(Er_i) = \frac{(p_{Er_i, T_2} - p_{full, T_2})}{\Delta_{full, T_2}} = 1 - \Delta_{Er_i, T_2} / \Delta_{full, T_2} \quad (14)$$

E.g., when turning off error Er_i and the result p_{Er_i, T_2} does not change, the error contribution is $c_r(Er_i) = 0$.

Ideally, we would quantify the error introduced by off-axis magnetic field by comparing to the application of parallel magnetic fields of different strength on both NVs in simulation. However, the exact transition frequencies that are asymmetrically distributed around the ZFS can only be recovered with a misaligned magnetic field in the simulation. Instead, we note that the experimental outcome on the electron spin with polarized nitrogen spin is equivalent to the case where the hyperfine interaction is turned off completely, because no population transferring terms $a_{ij}S_i \otimes I_j, i \neq j$ exist in \underline{A} for a perfectly aligned magnetic field. Hence, we can attribute the additional error that occurs for the polarized nitrogen spin case when $a_{ij}S_i \otimes I_j, i \neq j$ terms are present, solely to the misaligned magnetic field:

$$c_r(B \perp e_z) = c_r(HFS) - c_r(\text{unpol. } ^{14}\text{N}) \quad (15)$$

Finally, we can turn off all known error sources in the simulation simultaneously: crosstalk, leakage and the hyperfine interaction and calculate the difference to an experiment with only decoherence.

$$c_r(\text{residual}) = (1 - c_r(T_2)) - c_r(HFS, ct. + leak.) \quad (16)$$

These small residual errors scale with the microwave power in a range of $c_r(\text{residual}) = [0.9\% - 0.09\%]$ for the studied Rabi frequencies between 5-30 MHz. Thus, we attribute them mainly to unwanted dipolar interaction occurring during the microwave pulses.

The alternating readout described above for conversion from fluorescence to spin state can reject some of the leakage error. Although we verified in simulation that this effect is small for our magnetic field setting 2, we base Fig. 4d on a simulation without the additional π pulses in order to not underestimate leakage.

Our simulation of randomized benchmarking in Fig. 4c does not account for experimental SPAM errors like the imperfect charge state initialization or mixing of the initialized spin state. Such SPAM errors do not change the decay parameter p in randomized benchmarking, but will be represented in the amplitude fit parameters y_0, a . Hence, we use a free parameter that is multiplied onto our simulation result $\langle \sigma_z \rangle_{NV_{1+2}}$ and which is determined by least square minimization of the difference to the experimental data.

Error bars

Error bars on experimental fluorescence data are estimated from the photon shot noise as $1/\sqrt{n_{phot}}$ and are error propagated to the spin state domain. Errors on parameters extracted from fits are 1σ uncertainties.

Data Availability Statement

The datasets in this study are available from the corresponding author on reasonable request.

References

1. Arute, F., Arya, K., Babbush, R., Bacon, D., Bardin, J. C., *et al.* Quantum supremacy using a programmable superconducting processor. *Nature* **574**, 505–510 (2019).
2. Zhong, H. Sen, Wang, H., Deng, Y. H., Chen, M. C., Peng, L. C., *et al.* Quantum computational advantage using photons. *Science* **370**, 1460–1463 (2020).
3. Kim, Y., Eddins, A., Anand, S., Wei, K. X., van den Berg, E., Rosenblatt, S., Nayfeh, H., Wu, Y., Zaletel, M., Temme, K. & Kandala, A. Evidence for the utility of quantum computing before fault tolerance. *Nature* **618**, 500–505 (2023).
4. Bluvstein, D., Evered, S. J., Geim, A. A., Li, S. H., Zhou, H., *et al.* Logical quantum processor based on reconfigurable atom arrays. *Nature* **626**, (2023).
5. Waldherr, G., Wang, Y., Zaiser, S., Jamali, M., Schulte-Herbrüggen, T., Abe, H., Ohshima, T., Isoya, J., Du, J. F., Neumann, P. &

- Wrachtrup, J. Quantum error correction in a solid-state hybrid spin register. *Nature* **506**, 204–207 (2014).
6. Kelly, J., Barends, R., Fowler, A. G., Megrant, A., Jeffrey, E., *et al.* State preservation by repetitive error detection in a superconducting quantum circuit. *Nature* **519**, 66–69 (2015).
 7. Chen, Z., Satzinger, K. J., Atalaya, J., Korotkov, A. N., Dunsworth, A., *et al.* Exponential suppression of bit or phase errors with cyclic error correction. *Nature* **595**, 383–387 (2021).
 8. Foxen, B., Neill, C., Dunsworth, A., Roushan, P., Chiaro, B., *et al.* Demonstrating a Continuous Set of Two-Qubit Gates for Near-Term Quantum Algorithms. *Phys. Rev. Lett.* **125**, 120504 (2020).
 9. Ballance, C. J., Harty, T. P., Linke, N. M., Sepiol, M. A. & Lucas, D. M. High-Fidelity Quantum Logic Gates Using Trapped-Ion Hyperfine Qubits. *Phys. Rev. Lett.* **117**, 060504 (2016).
 10. Bartling, H. P., Yun, J., Schymik, K. N., van Riggelen, M., Enthoven, L. A., van Ommen, H. B., Babaie, M., Sebastiano, F., Markham, M., Twitchen, D. J. & Taminiou, T. H. Universal high-fidelity quantum gates for spin-qubits in diamond. *arXiv* 2403.10633 (2024).
 11. Bradley, C. E., Randall, J., Abobeih, M. H., Berrevoets, R. C., Degen, M. J., Bakker, M. A., Markham, M., Twitchen, D. J. & Taminiou, T. H. A Ten-Qubit Solid-State Spin Register with Quantum Memory up to One Minute. *Phys. Rev. X* **9**, 31045 (2019).
 12. van de Stolpe, G. L., Kwiatkowski, D. P., Bradley, C. E., Randall, J., Abobeih, M. H., Breitweiser, S. A., Bassett, L. C., Markham, M., Twitchen, D. J. & Taminiou, T. H. Mapping a 50-spin-qubit network through correlated sensing. *Nat. Commun.* **15**, 1–9 (2024).
 13. Dolde, F., Jakobi, I., Naydenov, B., Zhao, N., Pezzagna, S., Trautmann, C., Meijer, J., Neumann, P., Jelezko, F. & Wrachtrup, J. Room-temperature entanglement between single defect spins in diamond. *Nat. Phys.* **9**, 139–143 (2013).
 14. Dolde, F., Bergholm, V., Wang, Y., Jakobi, I., Naydenov, B., Pezzagna, S., Meijer, J., Jelezko, F., Neumann, P., Schulte-Herbrüggen, T., Biamonte, J. & Wrachtrup, J. High-fidelity spin entanglement using optimal control. *Nat. Commun.* **5**, 3371 (2014).
 15. Kelly, J., Barends, R., Campbell, B., Chen, Y., Chen, Z., *et al.* Optimal quantum control using randomized benchmarking. *Phys. Rev. Lett.* **112**, 240504 (2014).
 16. Vetter, P. J., Reisser, T., Hirsch, M. G., Calarco, T., Motzoi, F., Jelezko, F. & Müller, M. M. Gate-set evaluation metrics for closed-loop optimal control on nitrogen-vacancy center ensembles in diamond. *arXiv* 2403.00616 (2024).
 17. Boradjiev, I. I. & Vitanov, N. V. Control of qubits by shaped pulses of finite duration. *Phys. Rev. A - At. Mol. Opt. Phys.* **88**, 013402 (2013).
 18. Mihov, I. S. & Vitanov, N. V. Qubit dynamics driven by smooth pulses of finite duration. *arXiv* 1403.0035 (2024).
 19. Preskill, J. Quantum computing in the NISQ era and beyond. *Quantum* **2**, 1–20 (2018).
 20. Abobeih, M. H., Cramer, J., Bakker, M. A., Kalb, N., Markham, M., Twitchen, D. J. & Taminiou, T. H. One-second coherence for a single electron spin coupled to a multi-qubit nuclear-spin environment. *Nat. Commun.* **9**, 1–8 (2018).
 21. Haruyama, M., Onoda, S., Higuchi, T., Kada, W., Chiba, A., Hirano, Y., Teraji, T., Igarashi, R., Kawai, S., Kawarada, H., Ishii, Y., Fukuda, R., Tanii, T., Isoya, J., Ohshima, T. & Hanaizumi, O. Triple nitrogen-vacancy centre fabrication by C5N4Hn ion implantation. *Nat. Commun.* **10**, 4–9 (2019).
 22. Waldherr, G., Neumann, P., Huelga, S. F., Jelezko, F. & Wrachtrup, J. Violation of a temporal Bell inequality for single spins in a diamond defect Center. *Phys. Rev. Lett.* **107**, 090401 (2011).
 23. Grotz, B., Beck, J., Neumann, P., Naydenov, B., Reuter, R., Reinhard, F., Jelezko, F., Wrachtrup, J., Schweinfurth, D., Sarkar, B. & Hemmer, P. Sensing external spins with nitrogen-vacancy diamond. *New J. Phys.* **13**, (2011).
 24. Souza, A. M., Alvarez, G. A. & Suter, D. Experimental protection of quantum gates against decoherence and control errors. *Phys. Rev. A - At. Mol. Opt. Phys.* **86**, 1–4 (2012).
 25. Nielsen, M. & Chuang, I. *Quantum Computation and Quantum Information*. (Cambridge University Press).
 26. Chow, J. M., Gambetta, J. M., Córcoles, A. D., Merkel, S. T., Smolin, J. A., Rigetti, C., Poletto, S., Keefe, G. A., Rothwell, M. B., Rozen, J. R., Ketchen, M. B. & Steffen, M. Universal quantum gate set approaching fault-tolerant thresholds with superconducting qubits. *Phys. Rev. Lett.* **109**, 060501 (2012).
 27. Shi, F., Zhang, Q., Wang, P., Sun, H., Wang, J., Rong, X., Chen, M., Ju, C., Reinhard, F., Chen, H., Wrachtrup, J., Wang, J. & Du, J. Single-protein spin resonance spectroscopy under ambient conditions. *Science* **347**, 1135–1138 (2015).
 28. Neumann, P., Kolesov, R., Naydenov, B., Beck, J., Rempp, F., Steiner, M., Jacques, V., Balasubramanian, G., Markham, M. L., Twitchen, D. J., Pezzagna, S., Meijer, J., Twamley, J., Jelezko, F. & Wrachtrup, J. Quantum register based on coupled electron spins in a room-temperature solid. *Nat. Phys.* **6**, 249–253 (2010).
 29. Yudilevich, D., Stöhr, R., Denisenko, A. & Finkler, A. Mapping Single Electron Spins with Magnetic Tomography. *Phys. Rev. Appl.* **18**, 054016 (2022).
 30. Aslam, N., Waldherr, G., Neumann, P., Jelezko, F. & Wrachtrup, J. Photo-induced ionization dynamics of the nitrogen vacancy defect in diamond investigated by single-shot charge state detection. *New J. Phys.* **15**, (2013).
 31. Hopper, D. A., Lauigan, J. D., Huang, T. Y. & Bassett, L. C. Real-Time Charge Initialization of Diamond Nitrogen-Vacancy Centers for Enhanced Spin Readout. *Phys. Rev. Appl.* **13**, 024016 (2020).
 32. Marseglia, L., Hadden, J. P., Stanley-Clarke, A. C., Harrison, J. P., Patton, B., Ho, Y. L. D., Naydenov, B., Jelezko, F., Meijer, J., Dolan, P. R., Smith, J. M., Rarity, J. G. & O’Brien, J. L. Nanofabricated solid immersion lenses registered to single emitters in diamond. *Appl. Phys. Lett.* **98**, (2011).
 33. Groot-Berning, K., Raatz, N., Dobrinets, I., Lesik, M., Spinicelli, P., Tallaire, A., Achard, J., Jacques, V., Roch, J. F., Zaitsev, A. M., Meijer, J. & Pezzagna, S. Passive charge state control of nitrogen-vacancy centres in diamond using phosphorous and boron doping. *Phys. Status Solidi Appl. Mater. Sci.* **211**, 2268–2273 (2014).
 34. Geng, J., Shalomayeva, T., Gryzlova, M., Mukherjee, A., Santonocito, S., Dzhavadzade, D., Dasari, D. B. R., Kato, H., Stöhr, R., Denisenko, A., Mizuochi, N. & Wrachtrup, J. Dopant-assisted stabilization of negatively charged single nitrogen-vacancy centers in phosphorus-doped diamond at low temperatures. *npj Quantum Inf.* **9**, 1–8 (2023).
 35. Doi, Y., Fukui, T., Kato, H., Makino, T., Yamasaki, S., Tashima, T., Morishita, H., Miwa, S., Jelezko, F., Suzuki, Y. & Mizuochi, N. Pure negatively charged state of the NV center in n-type diamond. *Phys. Rev. B* **93**, 1–6 (2016).
 36. Magesan, E., Gambetta, J. M. & Emerson, J. Scalable and robust randomized benchmarking of quantum processes. *Phys. Rev. Lett.* **106**,

180504 (2011).

37. De Lange, G., Wang, Z. H., Ristè, D., Dobrovitski, V. V. & Hanson, R. Universal dynamical decoupling of a single solid-state spin from a spin bath. *Science* **330**, 60–63 (2010).
38. Bauch, E., Singh, S., Lee, J., Hart, C. A., Schloss, J. M., Turner, M. J., Barry, J. F., Pham, L. M., Bar-Gill, N., Yelin, S. F. & Walsworth, R. L. Decoherence of ensembles of nitrogen-vacancy centers in diamond. *Phys. Rev. B* **102**, 134210 (2020).
39. Bar-Gill, N., Pham, L. M., Jarmola, A., Budker, D. & Walsworth, R. L. Solid-state electronic spin coherence time approaching one second. *Nat. Commun.* **4**, 1743 (2013).
40. Huelga, S. F., Macchiavello, C., Pellizzari, T., Ekert, A. K., Plenio, M. B. & Cirac, J. I. Improvement of frequency standards with quantum entanglement. *Phys. Rev. Lett.* **79**, 3865–3868 (1997).
41. Geller, M. R. & Sun, M. Toward efficient correction of multiqubit measurement errors: Pair correlation method. *Quantum Sci. Technol.* **6**, (2021).
42. Wang, D. S., Fowler, A. G. & Hollenberg, L. C. L. Surface code quantum computing with error rates over 1%. *Phys. Rev. A - At. Mol. Opt. Phys.* **83**, 2–5 (2011).
43. Fowler, A. G., Mariantoni, M., Martinis, J. M. & Cleland, A. N. Surface codes: Towards practical large-scale quantum computation. *Phys. Rev. A - At. Mol. Opt. Phys.* **86**, (2012).
44. Genov, G. T., Schraft, D., Vitanov, N. V. & Halfmann, T. Arbitrarily Accurate Pulse Sequences for Robust Dynamical Decoupling. *Phys. Rev. Lett.* **118**, 133202 (2017).
45. Suter, D. & Álvarez, G. A. Colloquium: Protecting quantum information against environmental noise. *Rev. Mod. Phys.* **88**, 1–23 (2016).
46. Schwartz, I., Scheuer, J., Tratzmiller, B., Müller, S., Chen, Q., Dhand, I., Wang, Z. Y., Müller, C., Naydenov, B., Jelezko, F. & Plenio, M. B. Robust optical polarization of nuclear spin baths using Hamiltonian engineering of nitrogen-vacancy center quantum dynamics. *Sci. Adv.* **4**, 1–8 (2018).
47. Scheuer, J., Schwartz, I., Müller, S., Chen, Q., Dhand, I., Plenio, M. B., Naydenov, B. & Jelezko, F. Robust techniques for polarization and detection of nuclear spin ensembles. *Phys. Rev. B* **96**, 174436 (2017).
48. Jacques, V., Neumann, P., Beck, J., Markham, M., Twitchen, D., Meijer, J., Kaiser, F., Balasubramanian, G., Jelezko, F. & Wrachtrup, J. Dynamic polarization of single nuclear spins by optical pumping of nitrogen-vacancy color centers in diamond at room temperature. *Phys. Rev. Lett.* **102**, 057403 (2009).
49. Chakraborty, T., Zhang, J. & Suter, D. Optimization of a quantum control sequence for initializing a nitrogen-vacancy spin register. *Phys. Rev. A* **105**, 022622 (2022).
50. Bodenstedt, S., Jakobi, I., Michl, J., Gerhardt, I., Neumann, P. & Wrachtrup, J. Nanoscale Spin Manipulation with Pulsed Magnetic Gradient Fields from a Hard Disc Drive Writer. *Nano Lett.* **18**, 5389–5395 (2018).
51. Egger, D. J. & Wilhelm, F. K. Adaptive hybrid optimal quantum control for imprecisely characterized systems. *Phys. Rev. Lett.* **112**, 240503 (2014).
52. Werninghaus, M., Egger, D. J., Roy, F., Machnes, S., Wilhelm, F. K. & Filipp, S. Leakage reduction in fast superconducting qubit gates via optimal control. *npj Quantum Inf.* **7**, (2021).
53. Rembold, P., Oshnik, N., Müller, M. M., Montangero, S., Calarco, T. & Neu, E. Introduction to quantum optimal control for quantum sensing with nitrogen-vacancy centers in diamond. *AVS Quantum Sci.* **2**, (2020).
54. Müller, M. M., Said, R. S., Jelezko, F., Calarco, T. & Montangero, S. One decade of quantum optimal control in the chopped random basis. *Reports Prog. Phys.* **85**, (2022).
55. Glaser, S. J., Boscain, U., Calarco, T., Koch, C. P., Köckenberger, W., Kosloff, R., Kuprov, I., Luy, B., Schirmer, S., Schulte-Herbrüggen, T., Sugny, D. & Wilhelm, F. K. Training Schrödinger’s cat: Quantum optimal control: Strategic report on current status, visions and goals for research in Europe. *Eur. Phys. J. D* **69**, (2015).
56. Irber, D. M., Poggiali, F., Kong, F., Kieschnick, M., Lühmann, T., Kwiatkowski, D., Meijer, J., Du, J., Shi, F. & Reinhard, F. Robust all-optical single-shot readout of nitrogen-vacancy centers in diamond. *Nat. Commun.* **12**, (2021).
57. Robledo, L., Childress, L., Bernien, H., Hensen, B., Alkemade, P. F. A. & Hanson, R. High-fidelity projective read-out of a solid-state spin quantum register. *Nature* **477**, 574–578 (2011).
58. Pfaff, W., Hensen, B. J., Bernien, H., Van Dam, S. B., Blok, M. S., Taminiau, T. H., Tiggelman, M. J., Schouten, R. N., Markham, M., Twitchen, D. J. & Hanson, R. Unconditional quantum teleportation between distant solid-state quantum bits. *Science* **345**, 532–535 (2014).
59. Kimura, K., Onoda, S., Yamada, K., Kada, W., Teraji, T., Isoya, J., Hanaizumi, O. & Ohshima, T. Creation of multiple NV centers by phthalocyanine ion implantation. *Appl. Phys. Express* **15**, (2022).
60. Teraji, T., Yamamoto, T., Watanabe, K., Koide, Y., Isoya, J., Onoda, S., Ohshima, T., Rogers, L. J., Jelezko, F., Neumann, P., Wrachtrup, J. & Koizumi, S. Homoepitaxial diamond film growth: High purity, high crystalline quality, isotopic enrichment, and single color center formation. *Phys. Status Solidi Appl. Mater. Sci.* **212**, 2365–2384 (2015).
61. Suter, D. & Jelezko, F. Single-spin magnetic resonance in the nitrogen-vacancy center of diamond. *Progress in Nuclear Magnetic Resonance Spectroscopy* vols 98–99 50–62 at <https://doi.org/10.1016/j.pnmrs.2016.12.001> (2017).
62. Binder, J. M., Stark, A., Tomek, N., Scheuer, J., Frank, F., Jahnke, K. D., Müller, C., Schmitt, S., Metsch, M. H., Unden, T., Gehring, T., Huck, A., Andersen, U. L., Rogers, L. J. & Jelezko, F. Qudi: A modular python suite for experiment control and data processing. *SoftwareX* **6**, 85–90 (2017).
63. Qiskit contributors. Qiskit: An Open-source Framework for Quantum Computing. at <https://doi.org/10.5281/zenodo.2573505> (2023).
64. He, X. F., Manson, N. B. & Fisk, P. T. H. Paramagnetic resonance of photoexcited N-V defects in diamond. I. Level anticrossing in the 3A ground state. *Phys. Rev. B* **47**, 8809–8815 (1993).
65. Proctor, T., Rudinger, K., Young, K., Sarovar, M. & Blume-Kohout, R. What Randomized Benchmarking Actually Measures. *Phys. Rev. Lett.* **119**, 130502 (2017).
66. Wood, C. J. & Gambetta, J. M. Quantification and characterization of leakage errors. *Phys. Rev. A* **97**, 032306 (2018).
67. Balasubramanian, G., Chan, I. Y., Kolesov, R., Al-Hmoud, M., Tisler, J., Shin, C., Kim, C., Wojcik, A., Hemmer, P. R., Krueger, A.,

- Hanke, T., Leitenstorfer, A., Bratschitsch, R., Jelezko, F. & Wrachtrup, J. Nanoscale imaging magnetometry with diamond spins under ambient conditions. *Nature* **455**, 648–651 (2008).
68. Dolde, F., Fedder, H., Doherty, M. W., Noebauer, T., Rempp, F., Balasubramanian, G., Wolf, T., Reinhard, F., Hollenberg, L. C. L., Jelezko, F., Wrachtrup, J. & Nöbauer, T. Electric-field sensing using single diamond spins. *Nat. Phys.* **7**, 459–463 (2011).
 69. Jamonneau, P., Lesik, M., Tétienne, J. P., Alvizu, I., Mayer, L., Dréau, A., Kosen, S., Roch, J. F., Pezzagna, S., Meijer, J., Teraji, T., Kubo, Y., Bertet, P., Maze, J. R. & Jacques, V. Competition between electric field and magnetic field noise in the decoherence of a single spin in diamond. *Phys. Rev. B - Condens. Matter Mater. Phys.* **93**, 024305 (2016).
 70. Kehayias, P., Turner, M. J., Trubko, R., Schloss, J. M., Hart, C. A., Wesson, M., Glenn, D. R. & Walsworth, R. L. Imaging crystal stress in diamond using ensembles of nitrogen-vacancy centers. *Phys. Rev. B* **100**, 174103 (2019).
 71. Knauer, S., Hadden, J. P. & Rarity, J. G. In-situ measurements of fabrication induced strain in diamond photonic-structures using intrinsic colour centres. *npj Quantum Inf.* **6**, 2–7 (2020).
 72. Smeltzer, B., McIntyre, J. & Childress, L. Robust control of individual nuclear spins in diamond. *Phys. Rev. A - At. Mol. Opt. Phys.* **80**, 1–4 (2009).
 73. Chen, M., Hirose, M. & Cappellaro, P. Measurement of transverse hyperfine interaction by forbidden transitions. *Phys. Rev. B - Condens. Matter Mater. Phys.* **92**, 1–5 (2015).
 74. Goerz, M. H., Reich, D. M. & Koch, C. P. Optimal control theory for a unitary operation under dissipative evolution. *New J. Phys.* **16**, (2014).
 75. Wang, Z. H., De Lange, G., Ristè, D., Hanson, R. & Dobrovitski, V. V. Comparison of dynamical decoupling protocols for a nitrogen-vacancy center in diamond. *Phys. Rev. B - Condens. Matter Mater. Phys.* **85**, 57–61 (2012).
 76. Degen, C. L., Reinhard, F. & Cappellaro, P. Quantum sensing. *Rev. Mod. Phys.* **89**, 1–41 (2017).
 77. Tétienne, J. P., Rondin, L., Spinicelli, P., Chipaux, M., Debuisschert, T., Roch, J. F. & Jacques, V. Magnetic-field-dependent photodynamics of single NV defects in diamond: An application to qualitative all-optical magnetic imaging. *New J. Phys.* **14**, 0–15 (2012).
 78. Gupta, A., Hacquebard, L. & Childress, L. Efficient signal processing for time-resolved fluorescence detection of nitrogen-vacancy spins in diamond. *J. Opt. Soc. Am. B* **33**, B28 (2016).
 79. Waldherr, G., Beck, J., Steiner, M., Neumann, P., Gali, A., Frauenheim, T. H., Jelezko, F. & Wrachtrup, J. Dark states of single nitrogen-vacancy centers in diamond unraveled by single shot NMR. *Phys. Rev. Lett.* **106**, 157601 (2011).

Acknowledgments

We thank Michael Olney-Fraser, Thomas Unden, Philipp Neumann and Alex Retzker for helpful discussions. T.J. acknowledges support by the Foundation of German Business (sdw).

This work was funded by the German Federal Ministry of Research (BMBF) by future cluster QSENS (No. 03ZK110AB) and projects DE-Brill (No. 13N16207), SPINNING (No. 13N16210, No. 13N16209 and No. 13N16215), CoGeQ (No. 13N16101), DIAQNOS (No. 13N16463), quNV2.0 (No. 13N16707), QR.X (No. 16KISQ006) and Quamapolis (No. 13N15375), DLR via project QUASIMODO (No. 50WM2170), Deutsche Forschungsgemeinschaft (DFG) via Projects No. 386028944, No. 445243414, and No. 387073854 and Excellence Cluster POLiS (UP 33/1 Projekt-ID: 422053626). This project has also received funding from the European Union's HORIZON Europe program via projects QuMicro (No. 101046911), SPINUS (No. 101135699), C-QuENS (No. 101135359), QCIRCLE (No. 14 101059999) and FLORIN (No. 101086142), European Research Council (ERC) via Synergy grant HyperQ (No. 856432) and Carl-Zeiss-Stiftung via the Center of Integrated Quantum Science and technology (IQST) and project Utrasens-Vir (No. P2022-06-007).

Additional support was provided by JSPS KAKENHI (No. 21H04646, 24K01286), JST moonshot R&D Grant Number JPMJMS2062 and MEXT Q LEAP Grant Number JPMXS0118067395.

Author Contribution

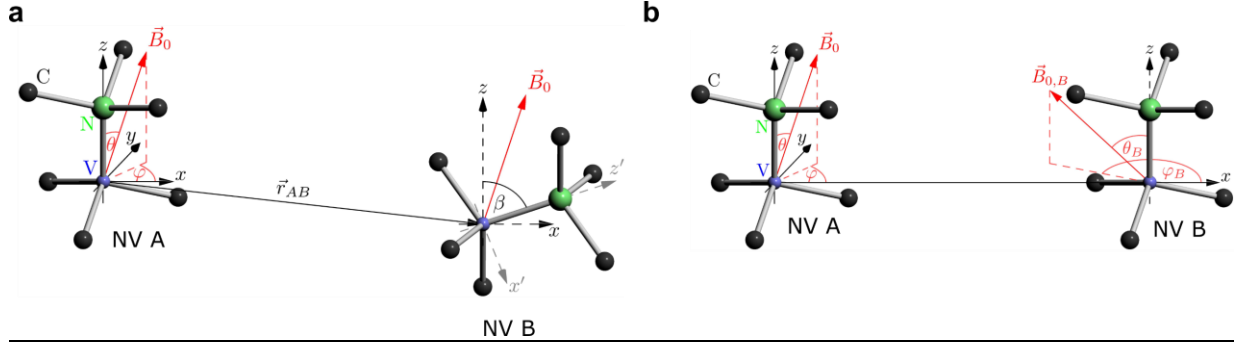
T.J., P.J.V., M.M.M. and F.J. conceived the experiment. T.T., S.O. fabricated, T.J., R.S., S.O. prepared and characterized the sample. T.J. wrote the code for the experiment and performed the measurements for the presented experimental data. F.F. and G.G. developed and analyzed the model and performed the simulations. T.J. and F.F. analyzed the data and wrote the manuscript. R.S.S., G.G., J.Z., S.O., T.C., M.M.M. and F.J. supervised the project. All authors read and contributed to the manuscript.

Competing Interests

The authors declare no competing interests.

Supplement

1: Magnetic field parameters



Suppl. Figure 1. Geometry of two NV register. (a) Physical geometry of coupled NVs in the crystal lattice, not to scale. The order in the gate sequence (labeled NV 1 and NV 2) is given along with geometry parameters in Suppl. Table 1. (b) Effective picture of the coupling. In this case, each NV is subject to a (unphysical) different magnetic field vector and the dipolar coupling is of zz type.

Most data presented is measured at the optimized magnetic field settings 2 of Suppl. Table 1. There, we use an aligned magnetic field on the control qubit (NV 2) for minimal population transfer to the nitrogen nuclear spins. On the misaligned target qubit this population transfer is much pronounced, but we can use the τ_1 degree of freedom to mitigate the issue (see Suppl. Note 4). In Fig. 4b, we also use the un-optimized setting 1 to illustrate the strong influence microwave crosstalk and leakage can have.

To obtain the magnetic field geometries, we determine the microwave transition frequencies by an ODMR measurement. For each magnetic field setting, the ODMR of two NV centers yields a set of four transition frequencies, where the lowest and highest frequencies form a pair as well as the two frequencies in between, which are associated to a magnetic field of higher misalignment with the NV center axis. Given these transition frequencies and the zero-field splitting D , one is able to calculate the absolute magnetic field value $\omega_{e,i}$ (in frequency units) and misalignment with each NV center using⁶⁷:

$$\omega_{e,i}^2 = \frac{1}{3}(v_{1,i}^2 + v_{2,i}^2 - v_{1,i}v_{2,i} - D_i^2) - E_i^2 \quad (S1)$$

$$H_i = \frac{7D_i^3 + 2(v_{1,i} + v_{2,i})(2(v_{1,i}^2 + v_{2,i}^2) - 5v_{1,i}v_{2,i} - 9E_i^2) - 3D_i(v_{1,i}^2 + v_{2,i}^2 - v_{1,i}v_{2,i} + 9E_i^2)}{9(v_{1,i}^2 + v_{2,i}^2 - v_{1,i}v_{2,i} - D_i^2 - 3E_i^2)} \quad (S2)$$

$$\cos(2\theta_i) = \frac{H_i - E_i \cos(2\varphi_i)}{D_i - E_i \cos(2\varphi_i)} \quad (S3)$$

where we defined H_i for a clear notation, $v_{1,i}$ and $v_{2,i}$ are the mentioned pair of transition frequencies, θ_i the misalignment angle between the axis of the considered NV center, i.e. the z-axis, and the magnetic field, φ_i the azimuthal angle (in the x-y-plane) and $i \in A, B$ the NV center to which the quantities are assigned. Note that the geometry in Suppl. Fig 1a is defined in terms of the physical NVs A and B, that can differ from their order in the gate sequence (NV 1 and NV 2).

Crystal strain can be divided into transversal strain E_i , and axial strain, which we model by including it into the zero-field parameters D_i ⁶⁸. Distinguishing both components from ODMR-like experimental data is not straightforward if considering a system of two NVs. Thus, we use the following methodology to determine D_i, E_i , making use of the assumption that the (absolute value of the) external magnetic field is constant for the closely located NVs:

As E_i is typically small ($\ll 1$ MHz) in bulk samples⁶⁸⁻⁷⁰ we are setting it to zero. For the magnetic field setting 2, we observe that Suppl. Equations S1-S3 do not lead to a physical solution when assuming a typical zero-field splitting at room temperature of $D/(2\pi) = 2870$ MHz⁶¹. Thus, we obtain the solution $D_A/(2\pi) = 2865.42$ MHz that minimizes axial strain on NV 2 and yields a valid magnetic field vector. Under the constraint that the absolute magnetic field is the same for both NV centers, this leads to an axial strain for NV 1 of $D_B/(2\pi) = 2867.27$ MHz. Our results for D_A, D_B are not significantly altered if a (pessimistic estimate) transversal strain of $E/(2\pi) \sim 1$ MHz⁷¹ is introduced, justifying our initial assumption of $E = 0$.

Using the same D_A, D_B obtained from the analysis of magnetic field setting 2 in the lower magnetic field setting 1, we observe a small, unexpected difference in the absolute magnetic field of both NVs, $|\omega_{e,A} - \omega_{e,B}|/\gamma_e = 1.1$ G.

Given the magnetic field amplitude and misalignment θ_i , we can calculate the remaining angle φ_A in Suppl. Fig 1a by making use of simple geometry. We simplify our notation and use $\theta = \theta_A$ and $\varphi = \varphi_A$ in the following. The angle between the direction of the magnetic field $\hat{\omega}_e = \hat{B}_0 = (\cos \varphi \sin \theta, \sin \varphi \sin \theta, \cos \theta)^T$ and the axis of NV center B, $\hat{n}_B = (0, \sin \beta, \cos \beta)^T$, is the misalignment angle θ_B :

$$\cos \theta_B = \hat{\omega}_e^T \cdot \hat{n}_B = \sin \varphi \sin \theta \sin \beta + \cos \theta \cos \beta \quad (\text{S4})$$

Note that we can find φ up to a relative minus sign that cannot be determined in a system of two NV centers only, due to its symmetry. At the same time, as we cannot differentiate between the signs, this implies that the dynamics are not affected by the choice of the sign.

Similarly, the geometry is not uniquely defined for θ , with two solutions θ and $\theta'_i = \pi - \theta_i$ for $\theta \in [0, \pi)$.

Furthermore, the angle between the NV center axes can take two possible values $\beta' = 109.47^\circ$ and $\beta = 180^\circ - \beta' = 70.53^\circ$ due to the crystal structure of diamond.

The (effective) dipole-dipole coupling strength is estimated by simulating the XY8-4 DEER experiment and adjusting the coupling strength to reproduce the experimentally observed τ_2 time. This is done individually for both magnetic field setups in Suppl. Note 3.

Suppl. Table 1. Parameters as chosen and estimated in the simulation. The computational basis of the qubit system (defined as $|0\rangle = |g\rangle, |1\rangle = |e_{1/2}\rangle$) employs the new spin eigenstates that are superpositions of the $m_s = |0\rangle, \pm|1\rangle$ electron spin states, with $|g\rangle$ referring to the spin ground state and $|e_{1/2}\rangle$ to the excited spin eigenstates (lower/higher transition frequency than ZFS).

| Magnetic field setting | Setting 1 ~60G | | Setting 2 ~100G | |
|--|------------------------------|------------------------------|------------------------------|------------------------------|
| NV center (gate sequence/physical order) | NV 1 / NV A | NV 2 / NV B | NV 2 / NV A | NV 1 / NV B |
| Zero-field splitting & axial strain $D/(2\pi)$ | 2865.42 MHz | 2867.27 MHz | 2865.42 MHz | 2867.27 MHz |
| Transversal strain E | 0 MHz | | | |
| Transition frequencies $f_i = \omega_i/(2\pi)$ (*): unused | 2932.5 MHz 2829.4 MHz (*) | 2751.8 MHz 2999.4 MHz (*) | 2571.0 MHz 3160.2 MHz (*) | 2990.8 MHz 2827.3 MHz (*) |
| Frequency separation $Min(f_i - f_j)$ | 66.9 MHz | | 163.5 MHz | |
| Absolute magnetic field $ B $ | 64.23 G | 63.101 G | 105.33 G | |
| Absolute magnetic field $ \omega_{e,i} /(2\pi) = \gamma_e B /(2\pi)$ | 180.01 MHz | 176.84 MHz | 295.18 MHz | |
| Misalignment θ_i | 73.42° | 45.53° | 3.58° | 74.08° |
| Quadrupole moment $Q/(2\pi)$ | -4.945 MHz ⁷² | | | |
| ¹⁴ N Off-Axis Hyperfine coupling $A_{xx}/(2\pi) = A_{yy}/(2\pi)$ | -2.62 MHz ⁷³ | | | |
| ¹⁴ N On-Axis Hyperfine coupling $A_{zz}/(2\pi)$ | -2.162 MHz ⁷² | | | |
| Angle between NV centers β | 70.53° | | | |
| Magnetic field orientation phi φ | 47.94° | | 172.73° | |
| Effective dipole-dipole coupling strength $\nu_{dip} = g/(2\pi)$ | 0.13994 MHz | | 0.11289 MHz | |
| Computational basis of qubit system $ 0\rangle, 1\rangle$ | $ g\rangle, e_2\rangle$ | $ g\rangle, e_1\rangle$ | $ g\rangle, e_1\rangle$ | $ g\rangle, e_2\rangle$ |
| Readout contrast α_i | 14.6 % | 14.6 % | 19.4 % | 10.7 % |

2: Simulation of two interacting NV centers

2a: System Hamiltonian

We start with the Hamiltonian⁶⁴ of a single, negatively charged, NV center of nitrogen isotope ^{14}N in its orbital ground-state $^3\text{A}_2$:

$$H^0 = \underbrace{DS_z^2 + \vec{\omega}_e \cdot \vec{S}}_{\equiv H^e} - \underbrace{QI_z^2 + \vec{\omega}_n \cdot \vec{I}}_{\equiv H^n} - \underbrace{\vec{S}\underline{A}\vec{I}}_{\equiv H^{\text{htc}}} \quad (\text{S5})$$

where D is the electronic zero-field splitting, Q the nuclear quadrupole moment, \vec{B}_0 the magnetic field at the positions of the NV center, \underline{A} the hyperfine tensor, which is diagonal, and $\vec{\omega}_{e/n} \equiv -\gamma_{e/n}\vec{B}_0$ with $\gamma_{e/n}$ being the gyromagnetic ratio of the electron/nuclear spin in angular frequency units (Hz rad/T). In the chosen coordinate system, the z-axis is aligned with the NV center axis.

We call $H^{e/n}$ the electron/nuclear Hamiltonian and H^{htc} the hyperfine coupling Hamiltonian. The respective spin operators $S_i(I_i)$, with $i \in \{x, y, z\}$, are defined to act on the electron (nuclear) states of the NV center only. Both the electron spin, due to the charge state NV^- of the NV center, and the nuclear spin, since we consider the ^{14}N isotope, are triplets ($S = I = 1$).

The system under consideration consists of two NV centers with distinct crystal axes (Suppl. Fig 1a represents magnetic field setting 2 with the stronger misaligned NV 1), interacting with each other via dipole-dipole coupling, that are exposed to microwave pulses of arbitrary shape. The total (noiseless) Hamiltonian is given by:

$$H(t) = \underbrace{H_{\text{NV}1}^0 + H_{\text{NV}2}^0 + H_{12}^{\text{dip}}}_{\equiv H^{\text{free}}} + H^{\text{mw}}(t) \quad (\text{S6})$$

where $H_{\text{NV}1}^0$ and $H_{\text{NV}2}^0$ are the single NV center Hamiltonians of NV centers 1 and 2, and H^{mw} the microwave Hamiltonian

$$H^{\text{mw}}(t) = \sum_{i=1,2} \sqrt{2} [\Omega_{i,x}(t) \cos(\omega_i t + \xi_i) + \Omega_{i,y}(t) \sin(\omega_i t + \xi_i)] \underbrace{\sum_{j=1,2} (S_{x,j} + \tilde{\gamma} I_{x,j})}_{\equiv H^{\text{control}}} \quad (\text{S7})$$

where $\Omega_{i,x}(t), \Omega_{i,y}(t)$ are time-dependent amplitudes (or control functions), that vary only slowly compared to the angular carrier frequencies ω_i . Phases of the carrier, generally set to zero, are denoted ξ_i , H^{control} is the control Hamiltonian and $\tilde{\gamma} = \gamma_e/\gamma_n$.

The dipole-dipole interaction Hamiltonian H_{12}^{int} is given by

$$H_{12}^{\text{int}} = g_0(r) [\vec{S}_1 \cdot \vec{S}_2 - 3(\vec{S}_1 \cdot \hat{r}_{12})(\vec{S}_2 \cdot \hat{r}_{12})] = g_0(r) \vec{S}_1 \underline{G}(\hat{r}_{12}) \vec{S}_2' \quad (\text{S8})$$

where \vec{r}_{12} is the displacement of NV center 1 from NV center 2 and $g_0(r_{12})$ the absolute coupling strength, depending on the distance r_{12} between the NV centers:

$$g_0(r_{12}) \equiv \frac{\mu_0 \hbar \gamma_e^2}{4\pi r_{12}^3} \quad (\text{S9})$$

We call $\underline{G}(\hat{\vec{r}}_{12})$ the geometric tensor. It does not depend on the distance r_{12} , but on the normalized relative position vector $\hat{\vec{r}}_{12}$ (c.f. Suppl. Fig. 1a).

To reflect the situation of the NV centers having misaligned axes by an angle β , which is necessary to achieve well-separated electron transition lines of the NV centers with respect to each other and thereby achieve individual control of the NV centers, the spin operators of NV 1 are rotated into the x', y', z' -frame where the axis of NV 1 coincides with the z' -axis (c.f. Suppl. Fig. 1a). Thereby, we ensure that both single NV center Hamiltonians take the same (simple) form. This is achieved by rotating the spin operators (and magnetic field) around the y -axis by $-\beta$:

$$\vec{S} \equiv \begin{pmatrix} S_x \\ S_y \\ S_z \end{pmatrix} \mapsto \vec{S}' = \begin{pmatrix} \cos \beta & 0 & -\sin \beta \\ 0 & 1 & 0 \\ \sin \beta & 0 & \cos \beta \end{pmatrix} \begin{pmatrix} S_x \\ S_y \\ S_z \end{pmatrix} \quad (\text{S10})$$

One can check that the simple form of the Hamiltonian is recovered as the electron zero-field term of NV 1 is transformed into the new coordinate system, e.g. for the zero-field splitting:

$$D(\cos(\beta)S_z + \sin(\beta)S_x)^2 = D(S'_z)^2 \quad (\text{S11})$$

Note, that, for consistency, the transformation has to be applied to all spin operators assigned to NV center 1. In this picture the NV centers are aligned with each other, but experience a different magnetic field and a modified geometric tensor $\underline{G}(\hat{\vec{r}}_{12})$.

As the NV centers are exposed to a constant magnetic field that is (generally) misaligned with their axes, their quantization axes are changed (in length and direction), which results in new eigenvalues and eigenstates of the Hamiltonian. As a consequence, the eigenstates of the electron Hamiltonian H^e do not coincide with the eigenstates of the $S_{z,2}, S'_{z,1}$ operators, but we can define new spin operators $\tilde{S}_{z,2}, \tilde{S}'_{z,1}$ that have the same eigenstates as H^e and take the usual form in the corresponding basis.

The dipole-dipole interaction is (typically) small compared to the electron transition frequencies ($g_0 \ll \omega_i$), so that a secular approximation can be applied, whereby small, non-diagonal elements in the dipole-dipole interaction Hamiltonian are neglected. This simplifies the dipole-dipole coupling (after the transformation) to:

$$H_{12}^{\text{int}} = g(\vec{r}_{12}, \beta, \vec{B}_0) \tilde{S}_{z,2} \tilde{S}'_{z,1} \quad (\text{S12})$$

where $g(\vec{r}_{12}, \beta, \vec{B}_0)$ is the effective coupling strength (in frequency units $v_{dip} = g/(2\pi)$).

By transforming the frame of NV center 1, transforming the spin operators into the basis of the electron eigenstates and performing the secular approximation, we have developed an effective picture of the two NV center system (c.f. Suppl. Fig. 1b).

2b: Simulation

For simulating the time dynamics of the system, we continue with NV Hamiltonians $H_{1/2}^0$, with the rotation by angle $-\beta$ applied on NV center 1, as above and compute the matrix T that diagonalizes the sum of the electron Hamiltonians $H^e \equiv H_1^e + H_2^e$, such that $T^\dagger H^e T$ is diagonal.

We apply the diagonalization matrix to the sum of the single NV Hamiltonians $H_1^0 + H_2^0$ and then add the effective dipole dipole coupling term in Suppl. Equation 8 to obtain the free Hamiltonian (in the effective picture):

$$H_{\text{free}} = T^\dagger(H_1^0 + H_2^0)T + H_{12}^{\text{int}} \quad (\text{S13})$$

If the magnetic field is static, the Hamiltonian of the system is given by H_{free} and therefore time-independent. In this case, the time evolution operator is calculated via the matrix exponential $U(t) = \exp(-iH_{\text{free}} t/\hbar)$ and then transformed into the rotating frame via:

$$U_{\text{rot}}(t) = V(t)U(t) \text{ with } V(t) = \exp(-iH_{\text{trans}} t) \quad (\text{S14})$$

where $H_{\text{trans}} \equiv \omega_1 S_{z,1}^2 + \omega_2 S_{z,2}^2$ is the Hamiltonian that generates the rotating frame transformation, $\omega_{1/2}$ are the angular carrier frequencies, ideally coinciding with the transition lines of the chosen qubit system ($2\pi f_i$ in Suppl. Table 1) and $S_{z,i}$ is the spin-z-operator defined to act on NV center i only, eg.:

$$S_{z,1} = S_z \otimes I$$

$$S_z = \begin{pmatrix} 1 & 0 & 0 \\ 0 & 0 & 0 \\ 0 & 0 & -1 \end{pmatrix} \quad (\text{S15})$$

If pulses are applied, the Hamiltonian contains time-dependent terms:

$$H_{\text{driven}}(t, t_0) = H_{\text{free}} + H^{\text{mw}}(t) \quad (\text{S16})$$

In order to calculate the time evolution from t_0 to t , we approximate the time-evolution via the Riemann summation method, whereby we evaluate the Hamiltonian at N discrete time points:

$$U(t, t_0) = \mathcal{T} \exp \left(-\frac{i}{\hbar} \int_{t_0}^t H_{\text{rot}}(t') dt' \right)$$

$$\approx e^{-i/\hbar H_{\text{rot}}(t_N)\tau} \dots e^{-i/\hbar H_{\text{rot}}(t_2)\tau} e^{-i/\hbar H_{\text{rot}}(t_1)\tau} \quad (\text{S17})$$

with $t_i = t_0 + i \tau$ and $\tau = (t - t_0)/N$, where $N = 20 \text{ GHz } (t - t_0)$ and \mathcal{T} is the time ordering operator.

To realize faster convergence, i.e. realize the same precision with larger time-steps, the Hamiltonian is transformed into the rotating frame (at every timestep) in which the Hamiltonian varies only slowly:

$$H_{\text{rot}}(t_i) = V_i^\dagger (H_{\text{free}} + H^{\text{mw}}(t_i) - H_{\text{trans}}) V_i \text{ with } V_i = V(t_i) \quad (\text{S18})$$

When dealing with sequences of pulses and free evolution, we multiply the respective unitaries time-orderly. We obtain readout results $R(\rho)$ via the POVM element $E_g(\{\alpha_i\})$, similar to the definition in ¹³, as:

$$\begin{aligned}
R(\rho) &= \text{Tr}_e [E_g \text{Tr}_n (U\rho U^\dagger)] - \text{Tr}_e [E_g \text{Tr}_n (X_{12} U\rho U^\dagger X_{12}^\dagger)] \\
E_g(\{\alpha_i\}) &= \frac{1}{\alpha_1 + \alpha_2} (\alpha_1 |g\rangle\langle g| \otimes \mathbb{1} + \alpha_2 \mathbb{1} \otimes |g\rangle\langle g|)
\end{aligned} \tag{S19}$$

where X_{12} is a π_x -pulse on NV center 1, followed by a π_x -pulse on NV center 2, $\text{Tr}_{e/n}$ is the trace of the electron/nuclear spins, and $\alpha_{1/2}$ is a contrast parameter, proportional to the spin contrast observed in experiment.

As we only read out diagonal elements in the measurement, the results are the same in the rotating frame as in the lab frame (since V_i is diagonal).

Within the simulation, if not stated otherwise, the electron state is perfectly initialized in the ground state, the nuclear state in the maximally mixed state (thermal state approximation). If the nuclear state is stated to be initialized, then it is initialized into its $m_I = 0$ state.

If not stated otherwise, the pulses are chosen to have a sinusoidal shape. E.g., for a π_x -pulse on NV center 1, the control functions are given by:

$$\Omega_{1,x}(t) = \Omega_{max} \sin(\pi \cdot t/t_\pi), \quad \Omega_{1,y}(t) = \Omega_{B,x}(t) = \Omega_{B,y}(t) = 0 \tag{S20}$$

where $\Omega_{max} = \frac{\pi}{2} \Omega_{rabi}$ is the peak amplitude of the envelope, $\Omega_{rabi} = \frac{\pi}{t_\pi}$, and t_π is the π pulse duration of the sine shaped pulse.

For evaluations of the gate fidelity, we use the definition of the average fidelity, given in ⁷⁴:

$$\begin{aligned}
F_{avg} &= \frac{1}{d(d+1)} \sum_{i,j=1}^d (\langle i|T^\dagger \mathcal{D}(|i\rangle\langle j|)T|j\rangle + \langle i|T^\dagger \mathcal{D}(|j\rangle\langle j|)T|i\rangle) \\
&= \frac{1}{d(d+1)} \left(\sum_{i=1}^d \langle i|T^\dagger \mathcal{D}(|i\rangle\langle i|)T|i\rangle + 2\text{Re} \sum_{i<j}^d \langle i|T^\dagger \mathcal{D}(|i\rangle\langle j|)T|j\rangle + \text{Tr} \mathcal{D}(\mathbb{1}) \right)
\end{aligned} \tag{S21}$$

Where T is the target quantum gate and \mathcal{D} is the dynamical map, i.e. the time evolution of the electron spins (under the influence of the nuclear spins):

$$\mathcal{D}(\rho) = \text{Tr}_n (U\rho U^\dagger) \tag{S22}$$

In our case, $d = 4$ and the $\{|i\rangle\}$ states are the basis of the qubit subspace. Note, that for the argument as given above, the fidelity is independent of the frame.

The randomized benchmarking sequences, used in the simulation, are the same as in the corresponding experiments. When sweeping the Rabi frequency, the set of pulses and the free evolutions are calculated for each Rabi frequency individually. When crosstalk and leakage are stated to be turned off, this means that the control Hamiltonian is modified to only act on the qubit levels of the desired NV center.

3: Single-qubit randomized benchmarking

To estimate the entangling qubit gate fidelity EPG_{2q} from the measured EPC of the gate set, we need to separate the error contribution of the single-qubit gates, as described in the Methods section:

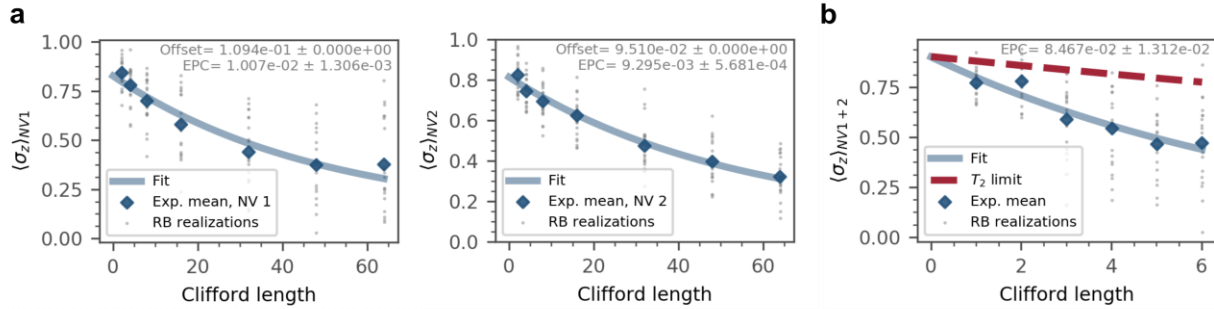
$$EPC = 1 - (1 - EPG_{2q})^{GPC_{2q}}(1 - EPG_{1q})^{GPC_{1q}} \quad (S23)$$

This is often done by measuring single-qubit randomized benchmarking on the sub systems (Suppl. Fig. 2a). Due to a particularity of our system, we take a slightly different approach here. We first note that due to limitations of our microwave hardware, we never apply pulses on both NVs at the same time. As a result of the unpolarized nitrogen spins, a single qubit rotation on NV1 thus can cause an unwanted phase pickup during the free evolution on NV2 and vice versa. This effect is neglected when carrying our single-qubit randomized benchmarking on a single NV only.

Instead, we determine the average effective single-qubit error $EPC_{1q} = 1 - (1 - EPG_{1q})^{GPC_{1q}}$ from a modified two-qubit randomized benchmarking experiment in Suppl. Fig. 2b: We strip out all entangling gates from the generated experiment ($GPC_{2q} = 0$) and append single qubit correction pulses to revert to the ground state (resulting modified $GPC_{1q} = 11.5$). On every qubit, the resulting experiment is still only containing random (single-qubit) Clifford operations – except for the free evolution that we treat as an error. We then determine EPC_{1q} from the fitted decay lifetime parameter $p = \exp\left(-\frac{1}{\tau_n}\right)$ as:

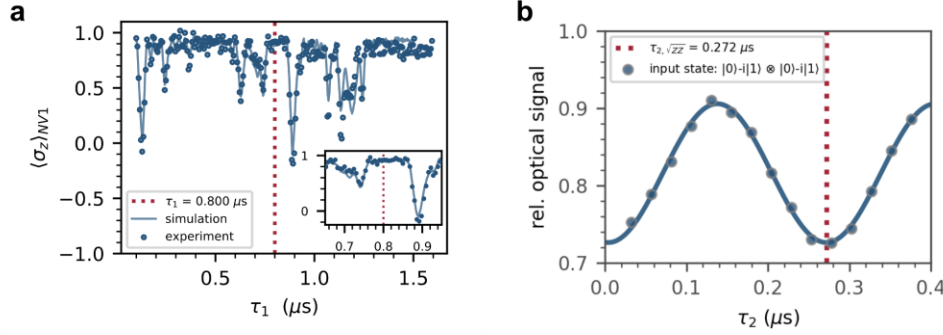
$$EPC_{1q} = (2^n - 1)/2^n(1 - p) = 0.085 \pm 0.013 \quad (S24)$$

With n the number of qubits in the Clifford sequence, here $n = 2$. This translates to an effective single-qubit fidelity of $F_{1q} = (99.23 \pm 0.12) \%$.



Suppl. Figure 2. Single-qubit randomized benchmarking. (a) Given the gate set $GPC_{1q} = 1.97$, we extract bare single-qubit gate fidelities of $F_{1q,NV1} = (99.49 \pm 0.56)\%$ and $F_{1q,NV2} = (99.53 \pm 0.49)\%$. Offset parameters are fixed by a separate measurement, as described in the Methods section. (b) Average single-qubit error $F_{1q} = (99.23 \pm 0.12)\%$ from modified two-qubit randomized benchmarking with stripped entangling gate.

4: Entangling gate dynamic & calibration



Suppl. Figure 3. Entangling gate calibration. (a) XY8-1 experiment performed with pulse spacing τ_1 on the misaligned target NV1 at magnetic field settings 2. (b) Measured repeated application of the \sqrt{ZZ} gate with varying τ_2 ($\tau_1=800$ ns, $n_{\text{rep}} = 4$, $\Omega_{\text{Rabi}}/(2\pi) = 22.97$ MHz) for calibration. The projection pulse after the \sqrt{ZZ} gates for both NVs is a $\pi_x/2$. The solid line is a fit from which we extract the $\tau_{2,\sqrt{ZZ}}$ that realizes our entangling gate.

In order to calibrate the duration of our entangling gate, we first analyze how it scales with the duration of our decoupling sequence and the choice of τ_1 and τ_2 .

To this end, we simplify the effective model Hamiltonian (Suppl. Equations S6, S12) further by assuming a dipole interaction along the $S_{z,1}, S_{z,2}$ operators:

$$\begin{aligned}
 H &= H_{NV1}^0 + H_{NV2}^0 + H^{\text{mw}} + H_{12}^{\text{int}} \\
 H_{NV1}^0 &= DS_{z,1}^2 + \Delta_1 S_{z,1} \\
 H_{NV2}^0 &= DS_{z,2}^2 + \Delta_2 S_{z,2} \\
 H^{\text{mw}} &= \sqrt{2}\{\Omega_{1,x}(t) \cos(\omega_1 t + \xi_1) + \Omega_{2,x}(t) \cos(\omega_2 t + \xi_2)\}(S_{x,1} + S_{x,2}) \\
 H_{12}^{\text{int}} &= gS_{z,1}S_{z,2}
 \end{aligned} \tag{S25}$$

where we denote as $S_{i,k}$ the operator S_i acting on the k -th NV center, $k=1,2$. The total Hamiltonian H^{total} can be obtained from the Hamiltonian in Suppl. Equation S12 by considering the effective dipolar coupling $g = 2\pi\nu_{\text{dip}}$ between the NV centers⁷⁵, with D the zero-field splitting of the NVs, $\Delta_k, k = 1,2$ is the effective detuning due to the Zeeman and hyperfine splittings, $\Omega_{1,x}(t)$ and $\Omega_{2,x}(t)$ characterize the Rabi frequencies of the microwave fields with angular frequencies ω_1 and ω_2 and initial relative phases ξ_1 and ξ_2 that we use to drive the two NV centers during the refocusing pulses. The subscript of each operator denotes which NV center it refers to, e.g., $S_{z,1}$ is equivalent to $S_{z,1} \otimes I$, i.e., a Kronecker product of S_z for NV1 and the identity operator I for NV2. Similarly, $S_{z,2}$ is equivalent to $I \otimes S_{z,2}$ and $S_{z,1}S_{z,2}$ denotes the operator $S_{z,1} \otimes S_{z,2}$.

We move to the rotating frame, defined by $\omega_1 S_{z,1}^2$ and $\omega_2 S_{z,2}^2$, apply the rotating wave-approximation, using that $\Omega_{1,2}(t) \ll \omega_{1,2}$, and obtain

$$H_{\text{rot}}^{NV1} = (D - \omega_1)S_{z,1}^2 + \Delta_1 S_{z,1} + \frac{\Omega_1(t)}{\sqrt{2}}S_{x,1} = \begin{pmatrix} D - \omega_1 + \Delta_1 & \frac{\Omega_1(t)}{2} & & 0 \\ \frac{\Omega_1(t)}{2} & \text{---} & \frac{\Omega_1(t)}{2} & \text{---} \\ & & \frac{\Omega_1(t)}{2} & \text{---} \\ 0 & \text{---} & \text{---} & D - \omega_1 - \Delta_1 \end{pmatrix} \tag{S26}$$

$$H_{rot}^{NV2} = (D - \omega_2)S_{z,2}^2 + \Delta_2 S_{z,2} + \frac{\Omega_2(t)}{\sqrt{2}} S_{x,2} = \begin{pmatrix} D - \omega_2 + \Delta_2 & \frac{\Omega_2(t)}{2} & 0 \\ \frac{\Omega_2(t)}{2} & 0 & \frac{\Omega_2(t)}{2} \\ 0 & \frac{\Omega_2(t)}{2} & D - \omega_2 - \Delta_2 \end{pmatrix} \quad (S27)$$

$$H_{rot}^{total} = H_{rot}^{NV1} + H_{rot}^{NV2} + g S_{z,1} S_{z,2}$$

$$H_{rot}^{total} = \begin{pmatrix} \delta_2 + \delta\delta_1 + g & \frac{\Omega_2(t)}{2} & 0 & \frac{\Omega_1(t)}{2} & 0 & 0 & 0 & 0 & 0 \\ \frac{\Omega_2(t)}{2} & \delta\delta_1 & \frac{\Omega_2(t)}{2} & 0 & \frac{\Omega_1(t)}{2} & 0 & 0 & 0 & 0 \\ 0 & \frac{\Omega_2(t)}{2} & \delta\delta_1 + \delta\delta_2 - g & 0 & 0 & \frac{\Omega_1(t)}{2} & 0 & 0 & 0 \\ \frac{\Omega_1(t)}{2} & 0 & 0 & \delta_2 & \frac{\Omega_2(t)}{2} & 0 & \frac{\Omega_1(t)}{2} & 0 & 0 \\ 0 & \frac{\Omega_1(t)}{2} & 0 & \frac{\Omega_2(t)}{2} & 0 & \frac{\Omega_2(t)}{2} & 0 & \frac{\Omega_1(t)}{2} & 0 \\ 0 & 0 & \frac{\Omega_1(t)}{2} & 0 & \frac{\Omega_2(t)}{2} & \delta\delta_2 & 0 & 0 & \frac{\Omega_1(t)}{2} \\ 0 & 0 & 0 & \frac{\Omega_1(t)}{2} & 0 & 0 & \delta_1 + \delta_2 - g & \frac{\Omega_2(t)}{2} & 0 \\ 0 & 0 & 0 & 0 & \frac{\Omega_1(t)}{2} & 0 & \frac{\Omega_2(t)}{2} & \delta_1 & \frac{\Omega_2(t)}{2} \\ 0 & 0 & 0 & 0 & 0 & \frac{\Omega_1(t)}{2} & 0 & \frac{\Omega_2(t)}{2} & \delta_1 + \delta\delta_2 + g \end{pmatrix} \quad (S28)$$

where we assume that the field frequency $\omega_1(\omega_2)$ is highly detuned from the transition frequencies of NV2 (NV1), so there is negligible cross-talk from pulses applied on NV1 on NV2 and vice versa. In addition, we take $\xi_1 = \xi_2 = 0$ for simplicity of presentation and without loss of generality. The matrix representation of $H_{rot}^{NV1}, H_{rot}^{NV2}$ is in the single qutrit basis of each of the NV centers, while H_{rot}^{total} is represented in the two-qutrit basis. In the experiment, the first driving field is approximately resonant with the $|0\rangle \leftrightarrow |-1\rangle$ transition on NV1 ($\delta_1 \equiv D - \omega_1 - \Delta_1 \ll \Omega_1(t), \delta\delta_1 \equiv D - \omega_1 + \Delta_2 \gg \Omega_1(t)$) and the second field - with the $|0\rangle \leftrightarrow |+1\rangle$ transition on NV2 ($\delta_2 \equiv D - \omega_2 + \Delta_2 \ll \Omega_2(t), \delta\delta_2 \equiv D - \omega_2 - \Delta_2 \gg \Omega_2(t)$). The Hamiltonian elements, which characterize the evolution of the states, which we can effectively address with the microwave fields (they do not have a very high frequency offset in the diagonal element of the Hamiltonian) are highlighted with dashed lines. Thus, the respective, reduced Hamiltonian, which characterizes the evolution that leads to our two-qubit gate is given by

$$H_{rot,reduced}^{total} = \begin{pmatrix} \delta_2 & \frac{\Omega_2(t)}{2} & \frac{\Omega_1(t)}{2} & 0 \\ \frac{\Omega_2(t)}{2} & 0 & 0 & \frac{\Omega_1(t)}{2} \\ \frac{\Omega_1(t)}{2} & 0 & \delta_1 + \delta_2 - g & \frac{\Omega_2(t)}{2} \\ 0 & \frac{\Omega_1(t)}{2} & \frac{\Omega_2(t)}{2} & \delta_1 \end{pmatrix} \quad (S29)$$

The detunings δ_1 and δ_2 typically cause dephasing but can be refocused by applying dynamical decoupling. The z-z coupling g allows us to apply the \sqrt{ZZ} gate, as evident from the analysis below. The Hamiltonian during free evolution without microwave pulses and the respective propagator are given by

$$H_{free} = \begin{pmatrix} \delta_2 & 0 & 0 & 0 \\ 0 & 0 & 0 & 0 \\ 0 & 0 & \delta_1 + \delta_2 - g & 0 \\ 0 & 0 & 0 & \delta_1 \end{pmatrix}, U_{free}(T_f) = \exp(-i H_{free} T_f) = \begin{pmatrix} e^{-iT_f \delta_2} & 0 & 0 & 0 \\ 0 & 1 & 0 & 0 \\ 0 & 0 & e^{iT_f(-\delta_1 - \delta_2 + g)} & 0 \\ 0 & 0 & 0 & e^{-i\delta_1 T_f} \end{pmatrix} \quad (S30)$$

We assume that the Rabi frequencies are much stronger than g , δ_1 and δ_2 , so we can neglect their effect during the refocusing pulses. Then, the Hamiltonians and propagators of the π pulses on NV 1 and NV 2 are respectively

$$H_{pulse}^{NV1} \approx \begin{pmatrix} 0 & 0 & \frac{\Omega_1(t)}{2} & 0 \\ 0 & 0 & 0 & \frac{\Omega_1(t)}{2} \\ \frac{\Omega_1(t)}{2} & 0 & 0 & 0 \\ 0 & \frac{\Omega_1(t)}{2} & 0 & 0 \end{pmatrix}, U_1(\theta_1) = \exp(-i H_{pulse}^{NV1} T_1) \approx \begin{pmatrix} \cos\left(\frac{\theta_1}{2}\right) & 0 & -i \sin\left(\frac{\theta_1}{2}\right) & 0 \\ 0 & \cos\left(\frac{\theta_1}{2}\right) & 0 & -i \sin\left(\frac{\theta_1}{2}\right) \\ -i \sin\left(\frac{\theta_1}{2}\right) & 0 & \cos\left(\frac{\theta_1}{2}\right) & 0 \\ 0 & -i \sin\left(\frac{\theta_1}{2}\right) & 0 & \cos\left(\frac{\theta_1}{2}\right) \end{pmatrix} \quad (S31)$$

$$H_{pulse}^{NV2} \approx \begin{pmatrix} 0 & \frac{\Omega_2(t)}{2} & 0 & 0 \\ \frac{\Omega_2(t)}{2} & 0 & 0 & 0 \\ 0 & 0 & 0 & \frac{\Omega_2(t)}{2} \\ 0 & 0 & \frac{\Omega_2(t)}{2} & 0 \end{pmatrix}, U_2(\theta_2) = \exp(-i H_{pulse}^{NV2} T_2) \approx \begin{pmatrix} \cos\left(\frac{\theta_2}{2}\right) & -i \sin\left(\frac{\theta_2}{2}\right) & 0 & 0 \\ -i \sin\left(\frac{\theta_2}{2}\right) & \cos\left(\frac{\theta_2}{2}\right) & 0 & 0 \\ 0 & 0 & \cos\left(\frac{\theta_2}{2}\right) & -i \sin\left(\frac{\theta_2}{2}\right) \\ 0 & 0 & -i \sin\left(\frac{\theta_2}{2}\right) & \cos\left(\frac{\theta_2}{2}\right) \end{pmatrix} \quad (S32)$$

where $\theta_1 = \Omega_1 T_1 = \pi$ and $\theta_2 = \Omega_2 T_2 = \pi$ (we assumed that the pulses are rectangular for simplicity of presentation and without loss of generality).

In order to characterize the gate, we consider a sequence of two instantaneous π pulses on each NV and analyze the evolution in the interaction basis of the pulses. The Hamiltonians in each free evolution period are given by:

Period 1: before the first π pulse on NV1:

$$H_{int,1} = H_{free} = \begin{pmatrix} \delta_2 & 0 & 0 & 0 \\ 0 & 0 & 0 & 0 \\ 0 & 0 & -g + \delta_1 + \delta_2 & 0 \\ 0 & 0 & 0 & \delta_1 \end{pmatrix}, t_1 = \frac{\tau_1}{2}, \quad (S33)$$

Period 2: after one π pulse on NV1, no π pulses on NV2:

$$H_{int,2} = U_{int,2} H_{free} U_{int,2}^\dagger = \begin{pmatrix} -g + \delta_1 + \delta_2 & 0 & 0 & 0 \\ 0 & \delta_1 & 0 & 0 \\ 0 & 0 & \delta_2 & 0 \\ 0 & 0 & 0 & 0 \end{pmatrix}, \text{ where } U_{int,2} = U_1(\pi), \quad t_2 = \frac{\tau_1}{2} - \tau_2 \quad (S34)$$

Period 3: after one π pulse on NV1, one π pulse on NV2:

$$H_{int,3} = U_{int,3} H_{free} U_{int,3}^\dagger = \begin{pmatrix} \delta_1 & 0 & 0 & 0 \\ 0 & -g + \delta_1 + \delta_2 & 0 & 0 \\ 0 & 0 & 0 & 0 \\ 0 & 0 & 0 & \delta_2 \end{pmatrix}, \text{ where } U_{int,3} = U_2(\pi)U_1(\pi), \quad t_3 = \frac{\tau_1}{2} + \tau_2 \quad (\text{S35})$$

Period 4: after two π pulses on NV1, one π pulse on NV2:

$$H_{int,4} = U_{int,4} H_{free} U_{int,4}^\dagger = \begin{pmatrix} 0 & 0 & 0 & 0 \\ 0 & \delta_2 & 0 & 0 \\ 0 & 0 & \delta_1 & 0 \\ 0 & 0 & 0 & -g + \delta_1 + \delta_2 \end{pmatrix}, \text{ where } U_{int,4} = U_1(\pi) U_2(\pi) U_1(\pi), \quad t_4 = \frac{\tau_1}{2} - \tau_2 \quad (\text{S36})$$

Period 5: after two π pulses on NV1, two π pulses on NV2:

$$H_{int,5} = U_{int,5} H_{free} U_{int,5}^\dagger = \begin{pmatrix} \delta_2 & 0 & 0 & 0 \\ 0 & 0 & 0 & 0 \\ 0 & 0 & -g + \delta_1 + \delta_2 & 0 \\ 0 & 0 & 0 & \delta_1 \end{pmatrix}, \text{ where } U_{int,5} = U_2(\pi)U_1(\pi) U_2(\pi)U_1(\pi), \quad t_5 = \tau_2 \quad (\text{S37})$$

The total evolution in the interaction basis is then given by

$$U_{int} = \exp(-i\sum H_{int,k} t_k) = \exp(i \xi_g) \begin{pmatrix} 1 & 0 & 0 & 0 \\ 0 & e^{iN_\pi g \tau_2} & 0 & 0 \\ 0 & 0 & e^{iN_\pi g \tau_2} & 0 \\ 0 & 0 & 0 & 1 \end{pmatrix} \quad (\text{S38})$$

where we used that $[H_{int,i}, H_{int,j}] = 0$ to obtain the first equality, $\xi_g = N_\pi [\frac{g}{2}(-\frac{\tau_1}{2} + \tau_2) + \frac{\tau_1}{2}(\delta_1 + \delta_2)]$ is an irrelevant global phase and N_π is the total number of applied pulses on each NV center, e.g., $N_\pi = 2$ in our example with two pulses or $N_\pi = 8$ for XY8-1 and $N_\pi = 16$ for XY8-2. Thus, in the following, we define the effective evolution time $t_{evol} = N_\pi \tau_2$.

For demonstrating the controlled oscillations of the \sqrt{ZZ} gate with XY8-1 decoupling on the Bloch sphere equator in Fig. 2, we use $\tau_1 = 3000$ ns. This choice allows to sweep the effective evolution time $t_{evol} = N_\pi \tau_2$ with large dynamic range (mind $-\tau_1/2 \leq \tau_2 \leq \tau_1/2$), but is not an optimal choice in terms of fidelity for two reasons:

First, shorter τ_1 allow to realize the same gate unitary with shorter total sequence length ($= N_\pi \tau_1$, independent of τ_2), and thus less decoherence. Consequently, for realizing the \sqrt{ZZ} unitary, τ_1 should be chosen close to $\tau_{1,min} = \frac{2}{4N_\pi v_{dip}} \sim 520$ ns for our $v_{dip} = 120$ kHz, $N_\pi = 8$ when using XY8-1. We note that using shorter τ_1 for our entangling gate, which requires a fixed $t_{evol} = N_\pi \tau_2$ with $\tau_2 \leq \tau_1/2$, is also possible by increasing N_π in the dynamical decoupling sequence, e. g., using XY8-2 that consists of 16 pulses. Decreasing the pulse spacing τ_1 should improve fidelity as the characteristic T_2 time of a decoupling sequence typically increases when the pulse separation is shorter^{44,45,76}.

Second, due to the misaligned magnetic field on the target qubit, population transfer to the nitrogen nuclear spin can occur. Since we can choose τ_1 freely (but not τ_2 that is set by v_{dip}), we use this degree of freedom to minimize such an unwanted interaction with the nitrogen spin. In Suppl. Fig. 3a, we probe the population transfer by initializing the target qubit into superposition and applying a standard XY8-1 experiment only on the target qubit with varying pi pulse spacing τ_1 . We observe that the simulation is

well reproducing the experimental data and find a $\tau_1 = 800$ ns that minimizes population transfer to the nitrogen spin.

After determining τ_1 , our gate calibration for τ_2 is carried out as follows: We initialize the input state $(|0\rangle - i|1\rangle) \otimes (|0\rangle - i|1\rangle)$ and apply the \sqrt{ZZ} gate sequence four times ($n = 4$) with varying τ_2 . Repeating the gate improves the accuracy of the calibration, as more oscillation periods are recorded for a τ_2 sweep. To the experimentally recorded oscillation (eg. in Suppl. Fig. 3b), we fit a sine and find the $\tau_{2,\sqrt{ZZ}}$ that is realizing minimal fluorescence, as expected from a quarter rotation (repeated $n = 4$ times) on the Bloch sphere equator.

In order to capture the gate dynamic accurately, we repeat the same calibration procedure to obtain a coupling parameter for our model. In addition to the experiment in in Suppl. Fig. 3b at magnetic field setting 2, we experimentally perform a calibration also at magnetic field setting 1 ($\tau_1=800$ ns, $n = 4$, $\Omega_{rabi}/(2\pi) = 15.51$ MHz, data not shown) and obtain a calibrated $\tau_{2,\sqrt{ZZ},B_1} = 212.6$ ns. We then simulate both calibration experiments and find the effective dipolar coupling parameters v_{dip} in Suppl. Table 1 that minimize the differences $|\tau_{2,exp,B_i} - \tau_{2,sim,B_i}|$.

5: Charge initialization & readout

Our charge initialization is based on a weak orange laser pulse and post-selection of the recorded spin readout photons. After the green (552 nm) spin initialization laser pulse, the charge state of a single NV in bulk diamond reaches a steady state occupation of typically $A(NV^-)/(A(NV^0) + A(NV^-)) \sim 0.7$ ³⁰. The orange laser probes the NV^- absorption with minimal overlap to the NV^0 absorption spectrum. At the same time, its weak power avoids ionization. Thus, more readout photons are expected during the orange laser pulse if both of the NVs are in the negative charge state. In Suppl. Fig. 4a, we measure readout photons per 3.5 ms long orange laser on our coupled NV quantum register. Due to the limited collection efficiency, the three expected Poissonian peaks $(NV^0,)$; $(NV^0,)$; (NV^-, NV^-) in the histogram overlap. For determination of the charge state, we fit a Poissonian model with free weighting parameters A_i and fitted mean rates λ_i :

$$p(n_{phot}) = A_{--}P(\lambda_{--}) + A_{-0}P(\lambda_{-0}) + A_{00}P(\lambda_{00}) \quad (S39)$$

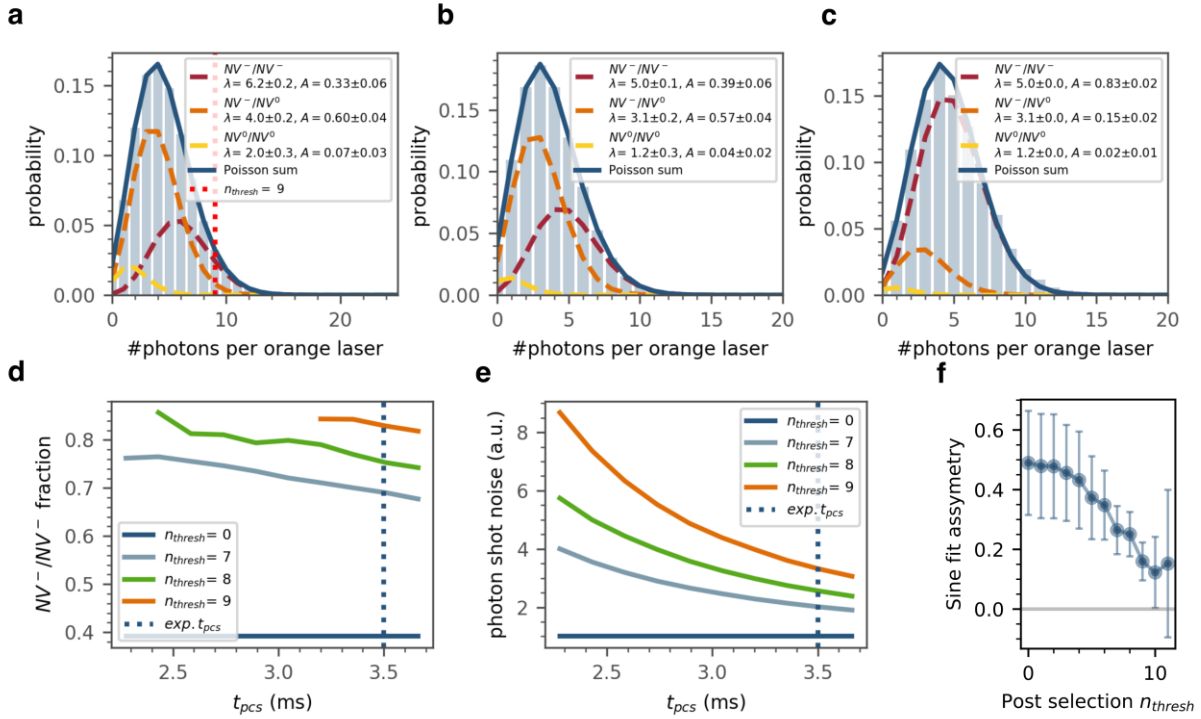
The extracted weights of the charge state slightly differ from the values $A_{00} = 0.09$, $A_{-0} = 0.42$, $A_{--} = 0.49$ expected for an independent combination of two bulk NVs. We speculate that a single charge shared between both NVs is more favorable in our system.

In Suppl. Fig. 4b we append another 2.9 ms long orange laser pulse to independently probe the charge state fidelity after the $t_{pcs} = 3.5$ ms long charge initialization laser pulse, without applying post selection yet. As expected, we recover charge state weights that are in agreement with the data in Suppl. Fig. 4a.

We then continue in Suppl. Fig. 4c to analyze only readout data for experimental shots that satisfy a threshold photon number n_{thresh} from the first initialization orange laser. After applying post-selection with the experimental settings ($t_{pcs} = 3.5$ ms, $n_{thresh}=9$) presented in Fig. 2,3, we measure an increase in (NV^-, NV^-) charge state initialization fidelity from (39 ± 6) % (no post-selection) to (83 ± 6) %.

In Suppl. Fig. 4d&e, we characterize the trade-off between higher charge state fidelity and readout noise: Better charge initialization can be reached for shorter t_{pcs} or higher n_{thresh} , but as more photons are discarded by the thresholding, the photon shot noise of the readout estimated as $1/\sqrt{n_{phots}}$ increases.

We tune the charge state by varying n_{thresh} in Suppl. Fig. 4f. Here, we utilize the σ_y component of the DEER oscillation as an alternative probe of the charge state and observe that its asymmetry reduces to (0.12 ± 0.12) when increasing to $n_{thresh} = 10$, indicating a clearly improved charge state initialization.



Suppl. Figure 4. Charge initialization & readout. **(a)** Histogram of photons collected during the $t_{pcs}=3.5$ ms orange charge initialization pulse. Before, the register is initialized with a $3 \mu s$ green laser pulse. Dashed lines are the single Poissonian contributions with fitted mean rates λ_i and weight A_i . The chosen thresholding photon number $n_{thresh} = 9$ used for charge initialization is shown as red dotted line. **(b)** Photon histogram collected during the 2.9 ms charge readout laser pulse after the charge initialization laser. **(c)** Photon histogram with same data as (b), but after applying post-selection to analyze only charge readout data if more than $n_{thresh} = 9$ photons are detected during the charge initialization pulse. The rates λ_i are fixed during fitting to the values extracted in (b). We conservatively estimate the error on the charge state fidelity by giving the uncertainty of the weight parameter A_{--} in (b). **(d)** NV^-/NV^- charge initialization fidelity measured for different length t_{pcs} of the gating window which counts photons during the charge initialization laser (same data set as in (b)&(c)). A shorter t_{pcs} shifts the Poissonian in the histogram to the left and thus increases charge state fidelity. Unstable fits are discarded. **(e)** Photon shot noise as calculated from the number of analyzed photons ($1/\sqrt{n_{phots}}$) and normalized to the noise without post-selection. Increasing the charge state fidelity comes at the cost of higher readout noise. **(f)** Asymmetry of the σ_y component of the DEER oscillation presented in Fig 2e while varying the post selection threshold parameter n_{thresh} .

6: SPAM and entangling gate fidelity in a magnetic field

Misaligning the magnetic field against the NV axis in the diamond lattice changes the effective decay rates into the new magnetic ground state levels that are superpositions of the aligned spin ground states⁷⁷. Consequently, spin initialization and readout of the NV are altered, as they depend on optical cycling through the NV's singlet state. Here, we estimate the SPAM error given in the main text caused by a reduced spin initialization in our (misaligned) magnetic field setting 2.

At our magnetic field setting 2, a reduced readout contrast is observed for the misaligned NV 1 in Suppl. Fig. 5a. We avoid the influence by different orientations of both NVs' optical dipoles by determining the maximum readout contrast for varying orientation of the linearly polarized green (552 nm) excitation laser by a $\lambda/2$ wave plate.

In Suppl. Fig. 5b, we verify that transformation of a 7 level rate equation model⁷⁷ agrees reasonably well with the experimentally observed relative Rabi contrast $\max(\text{contr}_{NV1}) / \max(\text{contr}_{NV2})$ at different absolute magnetic field values. The misalignment angle $\theta \approx 74^\circ$ of each datapoint is similar as in magnetic field setting 2, up to a precision of $\pm 2^\circ$.

We analyze the model with two sets of rates (see Suppl. Table 2):

1. Optical rates as given in⁷⁸. To calibrate the laser pump rate as the only free parameter, we minimize the difference to the experimental data. Comparing to our experimental data, we observe a deviation from the model.
2. Since the intersystem crossing rates are not straightforward to determine, we additionally adapt the rates from the ³E level to the singlet and minimize the difference to experimental data in parallel to the laser pump rate. The resulting rates fit better to our experimental data.

The same model allows us to estimate the SPAM error introduced by a reduced spin polarization. The electron spin initialization fidelity F_{init} is given by:

$$F_{init} = \frac{p_0}{p_0 + p_{-1} + p_{+1}} \quad (\text{S40})$$

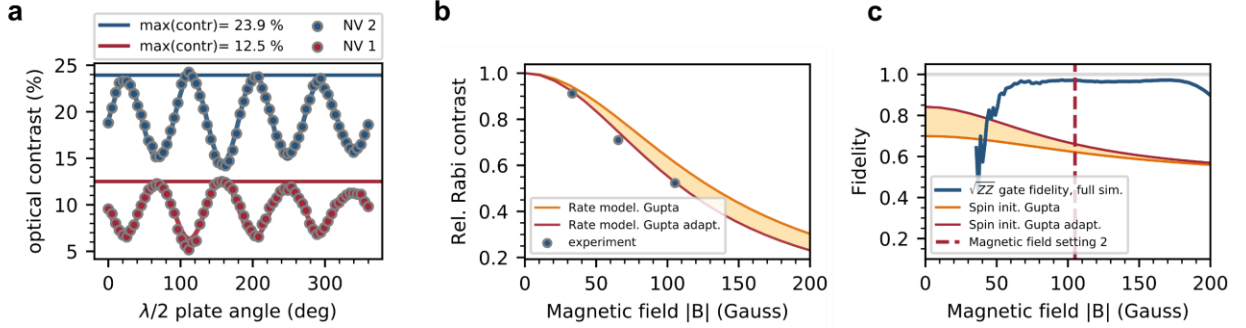
Note that the experimentally observed readout contrast at misaligned magnetic field in Suppl. Fig. 5a&b includes contributions from both the reduced spin polarization and the less efficient optical readout. To obtain the spin initialization fidelity, we determine the populations p_{m_s} of the $m_s = 0, \pm 1$ levels after a 3 us green laser and a waiting time of 1 us.

In Suppl. Fig. 5c, we plot the simulated spin initialization fidelity from Suppl. Equation S40 and the entangling gate fidelity (predicted like in Fig. 4e) for varying magnetic field. At zero field (equivalent to no misalignment), the predicted spin initialization fidelity (defined in the spin 1 manifold, mean of both set of rates) is 77 %. This value is lower than in experimental work ($\geq 92\%$ ⁷⁹, $(88 \pm 4)\%$ ²⁸), indicating that the available models might underestimate the absolute degree of spin polarization.

We estimate the SPAM error due to spin mixing to 17 % by dividing the simulated value (mean of both set of rates) at our magnetic field setting 2 by the value at zero field:

$$\text{err}_{SPAM,init} = \frac{1 - F_{init}(B)}{1 - F_{init}(B = 0)} \quad (\text{S41})$$

We observe a trade-off between higher gate fidelity but lower spin initialization fidelity when increasing the magnetic field. Depending on the application, diamond quantum registers with NVs of different orientations may be optimized towards higher entangling gate fidelity or reduced SPAM spin initialization error.



Suppl. Figure 5. SPAM error by spin mixing. (a) Optical contrast as measured from fits to Rabi oscillations on both NVs at different $\lambda/2$ wave plate angles with magnetic field setting 2. The maximum optical contrasts of both NVs is determined from the maximum value of a fitted empirical model (sum of two sines). (b) Relative Rabi contrast $\max(\text{contr}_{NV1}) / \max(\text{contr}_{NV2})$ at different absolute values of the magnetic field and misalignment angles $\theta_{NV1} \sim 74^\circ$, experimental precision $\pm 2^\circ$. The solid line is a simulation based on the rate model and transition rates in Suppl. Table 2. Circles are measurement data taken at different magnetic fields as described in (a). (c) Simulated \sqrt{ZZ} gate fidelity and spin initialization fidelity for different absolute values of the magnetic field and a misalignment angles $\theta_{NV1} = 74.08^\circ$, $\theta_{NV2} = 3.58^\circ$.

Suppl. Table 2: Rates used for modelling (as in ⁷⁷) the readout contrast and spin initialization fidelity in a misaligned magnetic field.

| Rates | Model Gupta ⁷⁸ , NV 1 | Model Gupta, adapted ISC |
|--------------------|----------------------------------|--------------------------|
| k_{57} | 92.9 MHz | 90.307 MHz |
| k_{67} | 92.9 MHz | 90.307 MHz |
| k_{47} | 11.2 MHz | 3.004 MHz |
| k_{71} | 4.9 MHz | 4.9 MHz |
| k_{72} | 2.03 MHz | 2.03 MHz |
| k_{73} | 2.03 MHz | 2.03 MHz |
| k_{41} | 66.08 MHz | 66.08 MHz |
| k_{52} | 66.08 MHz | 66.08 MHz |
| k_{63} | 66.08 MHz | 66.08 MHz |
| laser pump β | 1.215 | 1.938 |

7: Simulated gate fidelity

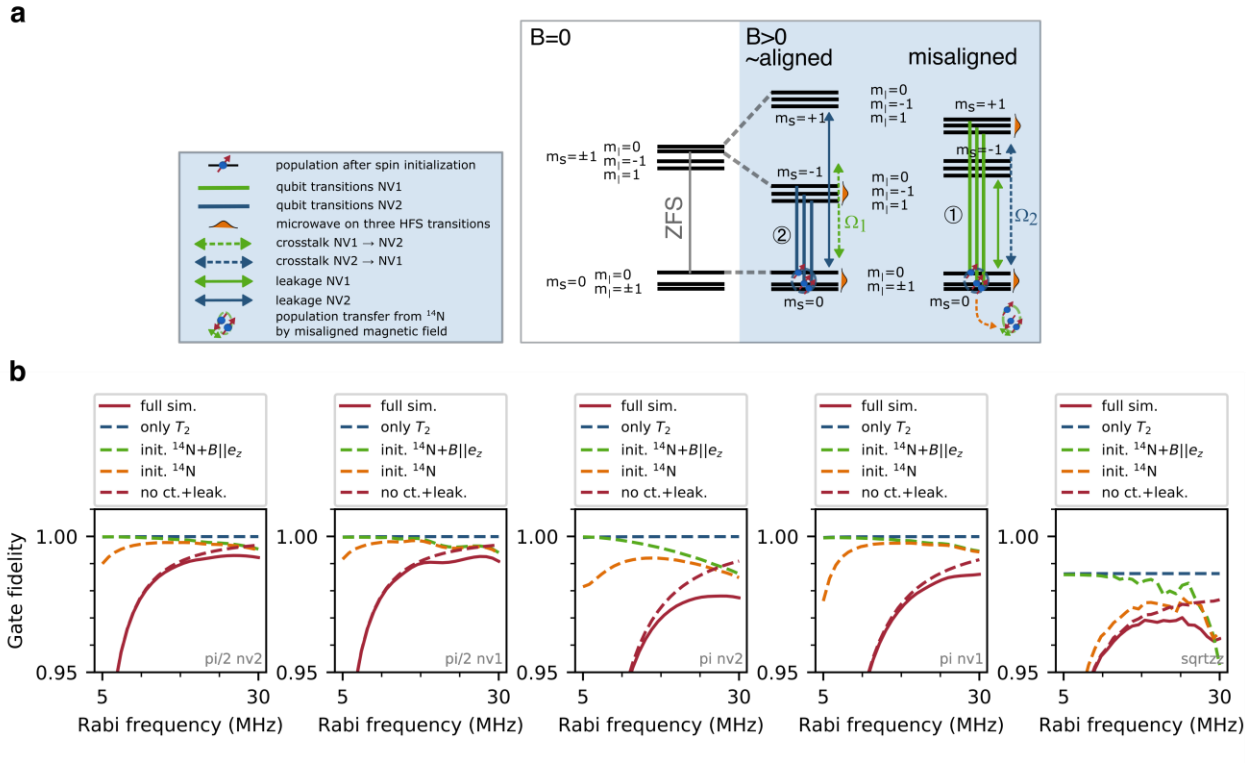
In the main text, we discuss the error sources determining the gate set fidelity. In Suppl. Fig. 6a, these errors are illustrated in the level structure of the coupled NV system. After spin initialization, both NVs are polarized into the $m_s = 0$ sublevels. Due to the unpolarized nuclear ^{14}N spins at ambient conditions, the initialized state is a mixed state with nearly equal classical probability of the nitrogen populations. However, our quantum register is not formed from the ^{14}N levels and initially the electron states are pure (after taking the partial trace).

After and during preparation of arbitrary register input states, multiple gate errors occur:

- The misaligned magnetic field can cause population transfer between the electron spin and the ^{14}N and thus decrease the electron spin polarization, especially during gate operations that contain dynamical decoupling pulses (see Suppl. Note 3).
- The unpolarized nuclear ^{14}N spin results in a random nuclear spin state at the beginning of every experimental shot. Due to the finite pulse power, detuned pulses suffer from imperfect driving of the three hyperfine lines, as indicated by the orange sketch of the pulse spectrum.
- Driving one of the $m_s = 0, -1$ (on NV 2) or $m_s = 0, 1$ (on NV 1) qubit transitions causes microwave crosstalk. Consequently, the dashed arrows represent unwanted population changes on the respective other qubit. Leakage transfers population out of the qubit subspace.

Note that all error sources may not only change populations, but also cause unwanted phase shifts.

In Fig. 4e, we predict the entangling gate fidelity of only the \sqrt{ZZ} gate from our model. We use the same simulation to give gate fidelities for the single-qubit gates of the gate set in Suppl. Fig. 6b. As the single-qubit pulses in our experiment don't employ dynamical decoupling, the fidelity improvement expected from polarized ^{14}N nitrogen spins is more pronounced. At high enough Rabi frequencies, we expect nearly no further improvement by aligning the magnetic field. Consequently, we anticipate that polarizing the nitrogen spins and mitigating crosstalk and leakage by optimal control could enable very high-quality single-qubit control in multi-NV diamond quantum registers.



Suppl. Figure 6. Gate errors. **(a)** Level scheme of the 3A_2 level of two NVs including Zeeman and ^{14}N hyperfine interaction. The error sources discussed in the main text are sketched. After spin initialization by the green laser, we obtain pure electron states indicated by blue dashed circles after tracing out the ^{14}N nuclear spins. During a gate, population transfer from the thermal nitrogen spin causes depolarization of the electron spin (green dashed ellipse). **(b)** Simulated gate fidelities for all gates (of phase X) of the gate set for different Rabi frequencies. Decoherence is considered as T_2 process as described in the Methods section and much smaller for the shorter single-qubit gates.